Geochimica et Cosmochimica Acta 367 (2024) 41–57

Contents lists available at ScienceDirect

Geochimica et Cosmochimica Acta

journal homepage: www.elsevier.com/locate/gca

Sulfur geochemistry of the Salitre Formation phosphorites: Implications for the role of microbial ecology and sulfur cycling in phosphogenesis on an Ediacaran carbonate platform

Cecilia Sanders [a,*], Theodore Present [b], Selva Marroquin [b], John Grotzinger [b]

[a] Department of Earth & Planetary Sciences, Johns Hopkins University, 3400 N Charles St, Olin Hall 301, Baltimore, MD 21218, United States
[b] Division of Geological and Planetary Sciences, California Institute of Technology, 1200 E California Blvd, MC 170-25, Pasadena, CA 91125, United States

ARTICLE INFO

Associate editor: Caroline P. Slomp

Keywords:
Phosphogenesis
Sulfur Isotopes
Microbial Metabolism

ABSTRACT

The distribution and activity of polyphosphate-accumulating sulfide oxidizing bacteria within marine sediments control the spatial distribution of sedimentary phosphorite formation in the modern ocean. In modern phosphogenetic settings, the concerted effect of microbial sulfide oxidation and microbial sulfate reduction in sediment pore waters is preserved in the sulfur isotope composition of trace sulfate in authigenic and early-stage diagenetic carbonate cements and phosphatic cements, as well as that of authigenic pyrite. If such variations in microbial sulfur metabolism controlled the spatial distribution of early phosphate mineralization in the geologic past, then one would expect to find differences between the sulfur isotope composition of cement-forming minerals in phosphatic and non-phosphatic facies of ancient sedimentary phosphate deposits. Here, we present paired measurements of the sulfur isotope composition of structural sulfate and structural sulfide in pore cements from co-occurring phosphatic and non-phosphatic facies of the Ediacaran Salitre Formation (Northeastern Brazil). The difference between $\delta^{34}S$ of trace structural sulfate in carbonate cements (CAS) or phosphate cements (PAS) and $\delta^{34}S$ of structural sulfide in pyrite or chromium-reducible sulfur (CRS), defined as $\Delta^{34}S$, provides a constraint on sulfur cycling within the pore waters from which the cements precipitated. In carbonate-cemented textures of the Salitre Formation, $\Delta^{34}S$ = 12 to 31 ‰. In phosphate-cemented textures, however, PAS and pyrite crystals had more similar sulfur isotope compositions: $\Delta^{34}S$ = −5–12 ‰. These values support the hypothesis that microbial sulfide oxidation was more prevalent in pore waters where phosphate mineralization occurred compared to pore waters where carbonate mineralization occurred – suggesting that microbial sulfide oxidation may have enabled the formation of sedimentary phosphorite on an Ediacaran carbonate platform, just as in modern phosphogenetic sites.

1. Introduction

There is broad consensus among biogeochemical researchers that phosphate-rich sedimentary deposits — phosphorites — are important to our understanding of past environments. Phosphorus is a vital nutrient, an essential component of biomass, and its concentration and accumulation in sediments at specific temporal horizons and in specific depositional environments has major consequences for global biogeochemical cycling throughout Earth history (Sundby et al., 1992; Cook, 1992; Canfield and Teske, 1996; Föllmi, 1996; Anschutz et al., 1998; Shields et al., 2004; Paytan and Mclaughlin, 2007; Papineau, 2010; Filippelli, 2011; Defforey and Paytan, 2018; Laakso et al., 2020). Phosphate minerals such as hydroxyapatite and carbonate-rich fluorapatite have, by virtue of their crystal structure and dissolution–recrystallization kinetics, the capacity to fossilize and preserve biological structures in exquisite detail, providing insight into the evolution of life (Xiao et al., 1998; Xiao and Knoll, 1999; Demidenko et al., 2003; Creveling et al., 2014; Bengtson et al., 2017; Sallstedt et al., 2018; Pruss et al., 2019). The spatial and temporal distributions of phosphorite provide insight into spatial and temporal variations in climate, ecology, and marine chemistry. Our understanding of the mechanisms by which environment and ecology effected phosphogenesis in the geologic past is yet imperfect; but in actively-forming modern phosphorites, it is possible to observe the mechanisms that control phosphate

* Corresponding author.
E-mail address: csande37@jhu.edu (C. Sanders).

https://doi.org/10.1016/j.gca.2023.12.033
Received 6 June 2023; Accepted 29 December 2023
Available online 30 December 2023

accumulation and mineralization *in situ* and through laboratory culture experiments. Modern phosphogenesis thus provides a model for phosphogenesis in the past which may be tested by examining ancient phosphorite deposits for geochemical and textural evidence of processes analogous to those in modern phosphogenetic environments.

There is a wealth of data that support a critical role for sulfur-metabolizing microorganisms in the formation of sedimentary phosphate deposits (phosphorite) at the modern seafloor. Sulfide-oxidizing microorganisms – specifically, polyphosphate-accumulating sulfide oxidizing bacteria including *Thiomargarita*, *Beggiatoa*, and *Thioplaca* - have been found in close association with phosphatic sediments of the Namibian shelf (Schulz and Schulz, 2005) and the Pacific margin of Costa Rica (Bailey et al., 2013). Phosphatic laminites from the Peruvian shelf are enriched with respect to organic molecules characteristic of sulfate-reducing bacteria and sulfide-oxidizing bacteria relative to non-phosphatic crusts in the same locality, and contain structural sulfate with $\delta^{34}S$ values which are lighter than that of ambient sea water to a degree consistent with fractionation via microbial sulfide oxidation (Arning et al., 2009). Laboratory cultures of model communities of polyphosphate-accumulating sulfide-oxidizing bacteria are observed to lyse their polyphosphate-accumulating vacuoles and release aqueous phosphate ions to surrounding media in response to anoxia and increased sulfide abundance (Schulz and Schulz, 2005; Brock and Schulz-Vogt, 2011; Crosby and Bailey, 2012). Furthermore, ^{33}P-radiotracer experiments have demonstrated the conversion of intracellular phosphate to extracellular apatite by living communities of giant sulfide bacteria cultured from Namibian shelf sediments - a process that did not occur in kill controls in which non-living cells failed to template apatite growth (Goldhammer et al., 2010).

All these data support the prevailing model that marine phosphogenesis occurs where communities of sulfate-reducing and sulfide-oxidizing bacteria effect elevated pore water phosphate concentrations and actively lower kinetic barriers to apatite mineral nucleation and growth under anoxic conditions.

However, ancient sedimentary phosphorites occur in a wider range of depositional environments than modern sedimentary phosphorites (reviewed by Sheldon, 1981; Föllmi, 1996; Southgate, 2005). They also exhibit a wider range of mineral growth textures and likely formed from pore waters and bottom waters derived from different ocean chemistries. Is it possible that the same microbially-mediated processes that facilitate modern phosphogenesis were also active in ancient phosphogenetic environments? If so, the isotopic composition of oxidized and reduced sulfur phases in pore cements of ancient sedimentary phosphorites might reflect the isotopic fractionation of oxidized and reduced sulfur pools by microbial metabolic activity during the formation of those phases.

Trace structural sulfate in carbonate minerals and phosphate minerals which precipitated from pore fluids should represent aqueous sulfate in those pore fluids during mineral nucleation and growth (Richardson et al., 2019). The isotopic composition of that pore water sulfate reflects the net effects of isotopic fractionation by sulfate-consuming reactions (microbial sulfate reduction and microbial sulfur disproportionation) and sulfate-producing reactions (microbial sulfide oxidation and microbial sulfur disproportionation) acting upon a pool of sulfate derived from seawater (Shields et al., 1999; Fike and Grotzinger, 2008; Wotte et al., 2012; Canfield, 2019). Likewise, the isotopic composition of sulfur in pyrite (FeS_2) should reflect the net effects of sulfide-generating reactions (microbial sulfate reduction and microbial sulfur disproportionation) and sulfide-consuming reactions (microbial sulfide oxidation and microbial sulfur disproportionation) prevalent in pore fluids near the redoxcline where aqueous Fe^{2+} is available to scavenge H_2S and form iron-sulfide minerals, namely pyrite.

The interplay of different microbial sulfur metabolisms operating at different rates and under different degrees of open-ness or closed-ness with respect to seawater may result in a wide range of $\delta^{34}S_{SO4} - \delta^{34}S_{H2S} = \Delta^{34}S$ recorded in pore cements. It may be impossible to reconstruct the precise network of biochemical pathways active in primary sediment pore waters from $\Delta^{34}S$ alone. It may, however, be possible to constrain the range of likely pathways which existed in phosphate mineralizing facies and compare them to the pathways which existed in non-phosphate mineralizing facies in the same geological place and time. If phosphogenesis was enabled by the metabolic activities of a given community of sulfur-metabolizing microorganisms, then - all other environmental parameters being the same - one would expect the isotopic signature $\Delta^{34}S$ of their metabolisms to be present in phosphatic pore cements and absent from non-phosphatic pore cements.

To this end, we measured $\delta^{34}S$ of structural sulfate and sulfide in mineral phases associated with both phosphatic and non-phosphatic textures of an ancient phosphorite: the Ediacaran Salitre Formation of Northeastern Brazil. The measured phases include carbonate cements (calcite and dolomite) in cross-stratified grainstone and crinkly laminated mudstone and phosphate cements (carbonate-rich fluorapatite or CFA) in the digitate stromatolite buildups which interfinger with grainstone and laminated mudstone facies. The geochemistry of these cements, precipitated from sediment pore waters on an Ediacaran carbonate platform, should reflect the geochemistry of those sediment pore waters and the processes that enabled either carbonate or phosphate mineralization - or else diagenetic modification. We interpret these new $\delta^{34}S$ data in their paragenetic context to determine whether they are consistent with biological sulfur cycling as observed in modern phosphogenetic environments.

2. Materials and methods

2.1. Geologic context

Geologic samples analyzed in this study were collected at various localities across the Irecê and Salitre paleobasins, sub-basins within a foreland basin system that existed in the interior of the São Francisco Craton during the Neoproterozoic Era (Martins-Neto et al., 2001; Kuchenbecker et al., 2011; Reis et al., 2016). Two major sedimentary rock units describe these sub-basin deposits, called the Una Group: (1) the Bebedouro Formation, <200 m in thickness, containing glaciogenic diamictites associated with the Marinoan glaciation (Guimarães et al., 2011; Caxito et al., 2012), and (2) the Salitre Formation, roughly 300–400 m in thickness, comprised of 4 members of roughly equal thickness which contain carbonate platform deposits in which siliciclastic content apparently increase with stratigraphic height (Misi and Kyle, 1994; Misi and Veizer, 1998; Misi et al., 2007). The phosphorite-bearing member of the Salitre Formation is its oldest, the Nova America member, comprised of massively bedded limestone and dolostone, featuring cross-stratified grainstone/rudstone, intraclast conglomerate, crinkly and planar laminated mudstones, and stromatolite buildup lithofacies (Sanders and Grotzinger, 2021). The phosphorite deposits of the Nova America member occur within some, but not all, of the laterally discontinuous stromatolite buildups which characterize this unit. The phosphatic stromatolites have a branching, digitate morphology and are composed primarily of micro-to-cryptocrystalline carbonate fluorapatite or CFA cements, which bind interlaminated organic matter and carbonate peloids and ooids (Shiraishi et al., 2019; Sanders and Grotzinger, 2021; Sanders et al., 2023). Inter-stromatolite fill is comprised of carbonate peloids and ooids cemented by carbonate minerals only. Digitate stromatolite buildups interfinger on meter- and 10s-of-meter scales with cross-stratified grainstone and occasionally planar- and crinkly-laminated mudstone (Caird et al., 2017; Sanders and Grotzinger, 2021). Non-phosphatic (carbonate-only) stromatolites have a similar spatial distribution, occurring both independently and alongside or within principally phosphatic stromatolite buildups (Sanders and Grotzinger, 2021).

Previous studies have described the paragenesis of the Salitre Formation's phosphorite deposits in detail, based on optical petrography, elemental mapping, and carbon and oxygen isotopic compositions and

clumped-isotope constrained paleotemperatures (Caird et al., 2017; Sanders et al., 2023). These studies concluded that the spatial distribution of phosphatic CFA cements was more consistent with phosphate enrichment by authigenic or very early diagenetic processes than with pervasive diagenesis by deep circulating fluids or meteoric water. Though the Salitre phosphorites are ~647–585 million years old and have experienced kilometers of burial and uplift, geochemical and textural data both suggest that later-stage diagenesis occurred under low water–rock ratio conditions and that — given the absence of indicators of diagenetic overprinting of the carbon and oxygen isotopes of carbonate in both CFA and carbonate cements — diagenetic resetting of the isotopic composition of structural sulfur in cement fabrics was likely limited (Sanders and Grotzinger, 2021; Sanders et al., 2023). The timing of pyrite mineralization relative to the origin of the carbonate and CFA cements is more difficult to constrain. However, we and previous workers (Caird et al., 2017; Sanders et al., 2023) observe that pyrite and oxidized pseudomorphs thereafter appear as a minor "intergrown" phase within the matrix of phosphatic and non-phosphatic lithofacies. The pyrites are not spatially associated with fractures or stylolites, but rather distributed diffusely through cement matrices. This is consistent with a scenario in which pyrite formed throughout early cementation/lithification alongside carbonate and CFA cements, with later diagenetic alteration evidenced by oxidized zoning of primary or early diagenetic crystals and *not* younger un-oxidized pyrite crystals cross-cutting primary fabrics.

For this study, we selected a range of hand samples from within the phosphorite interval of the Salitre Formation's Nova America member. Samples were taken from measured outcrops in the Irece and Salitre paleobasin regions (Figs. 1 and 2) and represent both phosphatic and non-phosphatic cement-forming environments within the same stratigraphic interval. Phosphatic textures include CFA-cemented laminae within digitate stromatolites. Non-phosphatic textures include carbonate-cemented grainy inter-stromatolite fill associated with phosphate-rich digitate stromatolite buildups, as well as carbonate-cemented grainstone immediately adjacent to stromatolite buildups, and carbonate-cemented mudstones. Representative images and illustrations of these textures are presented in Fig. 3.

2.2. Selection of samples

This study required the integration of many different techniques for the extraction, purification, and isotopic analysis of sulfur in specific co-occurring mineral phases/reservoirs in natural geologic samples, summarized in Fig. S1. Mineral phases analyzed included the micro- to cryptocrystalline carbonate fluorapatite (CFA) cement matrix of phosphatic digitate stromatolites, the micritic and interlocking anhedral mosaic calcite and dolomite cement matrix of non-phosphatic stromatolites and inter-stromatolite grainstone, and minor pyrite intergrown with and cross-cutting the carbonate and CFA cements.

Mineral fabrics suitable for such texturally-specific sulfur isotope analysis were selected via optical petrography, Raman microscopy, and paired scanning electron microscopy and energy dispersive spectrometry (SEM/EDS) of petrographic thin sections and their corresponding offcuts/billets, previously prepared for the characterization of the Salitre Formation's formation and paragenesis (Sanders et al., 2023). These elemental and mineralogical analyses were performed in Caltech's Division of Geological and Planetary Sciences Analytical Facility, using an optical petrographic microscope, Renishaw InVia Confocal Raman Microscope with 514 nm primary laser, and Zeiss 1550VP Field Emission SEM using 15–20 KeV electron beam. Compositional maps, annotated thin section photomicrographs, etc. are presented in the results of previous studies (Sanders and Grotzinger, 2021; Sanders et al., 2023). Thus, we identified and collected images and compositional maps of microcrystalline CFA and carbonate mineral cement fabrics which were devoid of late stage diagenetic features (such as fractures and associated sparry cements) on sub-millimeter spatial scales, and which were established by carbon and oxygen isotopic data as unlikely to have undergone diagenetic overprinting by meteoric or hydrothermal fluids. Table 1 summarizes the mineralogy and microtextural associations ("microfacies") of all samples selected for this study.

We used the characterization of sample thin sections to select corresponding fabrics in their offcuts for texture-specific, mm-scale drilling to collect powders (i.e., comprised of particles with 10s-of-μm diameters or less). Fabrics which were homogeneous over a spatial scale of ~1 cm were reduced to gravels/granules using a rock hammer, then reduced to powders using an agate ball mill. Drilled and milled sample fabrics

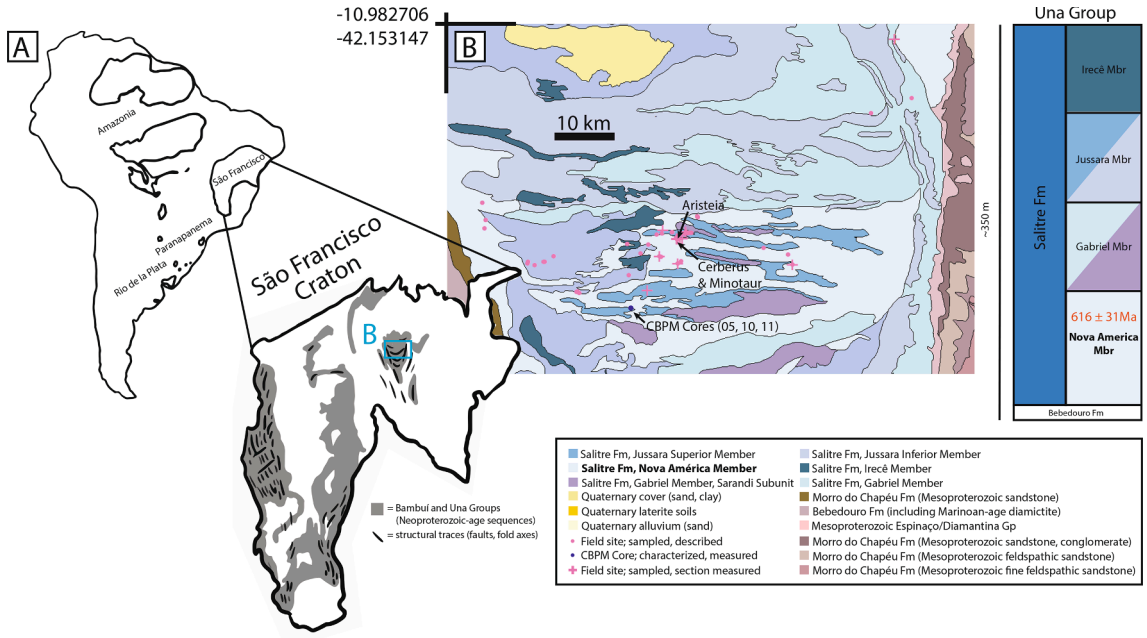

Fig. 1. Geographical and stratigraphic context of presented geochemical measurements. (a) Map depicting the location of the São Francisco Craton relative to nearby cratonic remnants (Cordani and Sato, 1999; Alkmim and Martins-Neto, 2012; Reis et al., 2017). (b) Geologic map of region indicated in (a), and stratigraphy of the Una Group (Dalton de Souza et al., 2003; Fonseca et al., 2014).

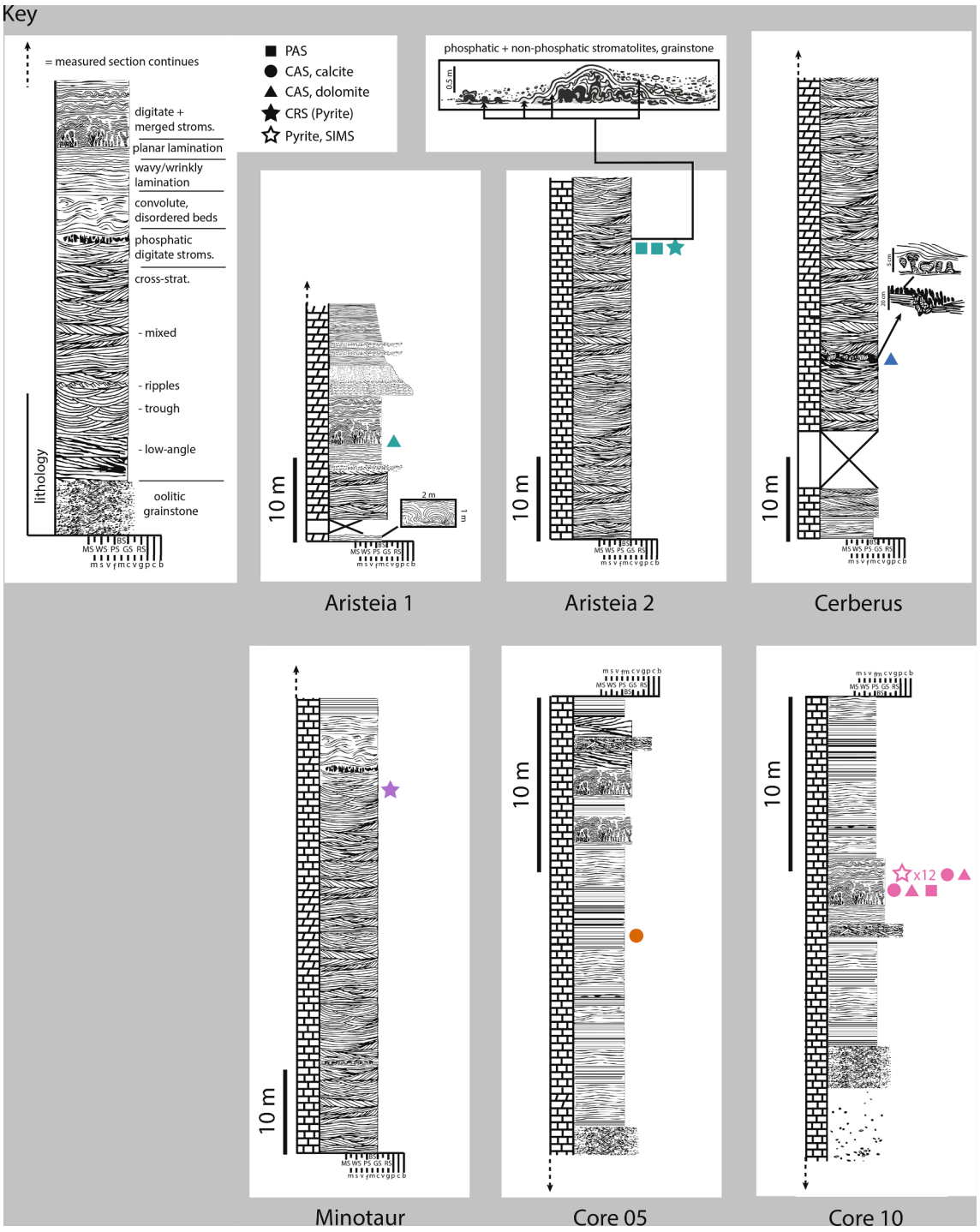

Fig. 2. Simplified stratigraphic columns from the Aristeia, Cerberus, and Minotaur Localities, as well as from CBPM Cores 5 and 10. In the Aristeia column, digitate stromatolite buildups are depicted in which CFA cements – colored red –are prevalent at the base/core of the buildup, and are less common in the more merged/disordered laminated textures (Sanders and Grotzinger, 2021; Sanders et al., 2023). All columns occur within the Nova America Member of the Salitre Formation within the Una Group. Shapes adjacent to the columns indicate the location in each stratigraphic column from which geochemical samples and their corresponding thin sections were collected.

which yielded more than several mg of powder (of which there was at least 1 from each locality) had their bulk mineralogy verified via X-ray powder diffraction using the Caltech Crystallography Facility's Panalytical X'Pert Pro instrument. Calcite, dolomite, and CFA were the only minerals present in the sample powders above the instrumental limit of detection. The presence of trace pyrite associated with the targeted CFA and carbonate cements was ascertained via spectroscopy and reflected light microscopy of thin sections.

Powder extracted from fabrics consisting of carbonate cement with minor pyrite was allocated for extraction of trace carbonate-associated sulfate (CAS) and extraction of pyrite sulfur as chromium-reducible sulfur (CRS). Powder extracted from fabrics consisting of CFA cement with minor pyrite was allocated for extraction of phosphate-associated sulfate (PAS) and extraction of pyrite sulfur as CRS. Pyrite from those powder samples for which CRS extraction yielded less than 4 μg S were analyzed via Secondary Ion Mass Spectrometry, with host fabrics

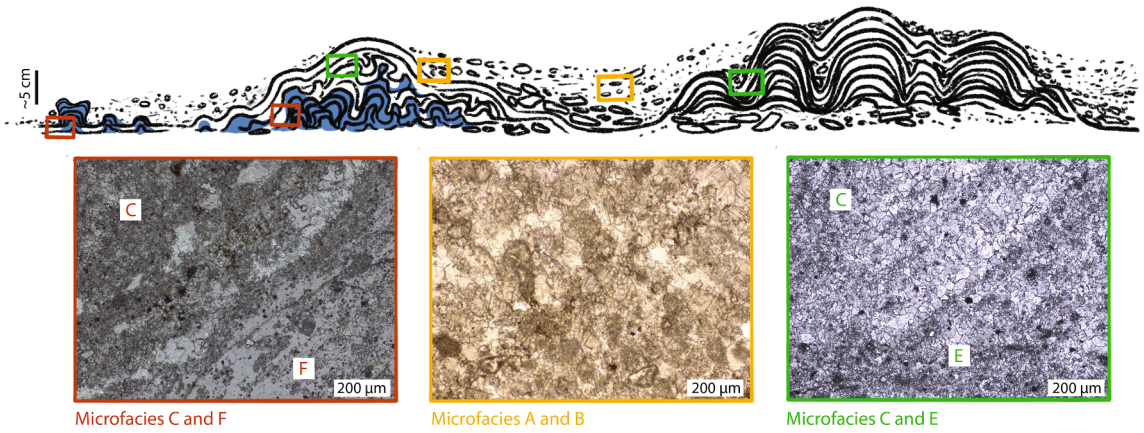

Fig. 3. Illustration of distinct microtextural associations ("microfacies") examined in this study, and example thin section photomicrographs thereof. Microfacies A = carbonate-cemented grainstone, B = carbonate-cemented grainstone adjacent to phosphatic digitate stromatolite buildup, C = carbonate-cemented grainy inter-stromatolite fill, D = carbonate-cemented laminated mudstone, E = carbonate-cemented stromatolite laminae, and F = CFA-cemented stromatolite laminae. Blue shading indicates spatial distribution of phosphatic cements (i.e., Microfacies F). Colored boxes indicate textural associations of each microfacies at the outcrop/hand sample scale and example thin section photomicrographs of mineral fabrics therein. Red boxes = C and F, yellow boxes = A and B, and green boxes = C and E. D is not pictured, due to its similarity to A and B (yellow boxes).

imaged via SEM and optical microscopy. See below for all extraction and purification protocols, and sulfur isotope mass spectrometry methods.

2.3. Preparation of samples for sulfur isotope analysis

2.3.1. Extraction of carbonate-associated sulfate (CAS)

Structural sulfate in the carbonate mineral lattice is a trace component of the rock, with low concentrations on the order of hundreds to thousands of ppm for most abiogenic carbonates (Staudt and Schoonen, 1995). Because the abundance of the target analyte is so low, extraction and purification protocols, adaptfed from previous studies of trace sulfate in carbonate undertaken in the same laboratory facilities (Paris et al., 2013, 2014; Present et al., 2015, 2019), were performed under cleanroom conditions to minimize contamination of samples from background sulfate.

2.3.1.1. 10 % NaCl rinse to remove easily soluble sulfate. Twelve powder samples comprised of near-pure carbonate minerals (i.e., calcite and dolomite), as well as a consistency standard derived from modern coral, were weighed into microcentrifuge tubes with 10 % NaCl solution, and sonicated for >8 h. Samples and standard were then centrifuged at 13,200 rpm for five minutes, and NaCl supernate removed and discarded via micropipette. Samples and standard were then rinsed 3 times with deionized and filtered Milli-Q water (each rinse consisting of agitation/resuspension of the powders in Milli-Q water, followed by centrifuging, and removal of supernate). Powders were resuspended in Milli-Q water, transferred to acid-cleaned microcentrifuge tubes, and dried at 65 °C for >8 h. This protocol is adapted from that of Present et al. (Present et al., 2015, 2019).

2.3.1.2. Acid digestion of carbonate minerals. 0.5 N HCl was added to each vial of dried powder sample and 2 additional empty vials ("blanks"). Samples were allowed to react for 4.25 h at ambient lab temperatures (~25 °C), being periodically agitated or resuspended every 30 min. Then, samples and blanks were centrifuged for 5 min at 13,200 rpm, and their supernate transferred to acid-cleaned PTFE Savillex vials. Acid-insoluble residues were dried at 65 °C for >8 h and stored. At this time, an additional seawater standard was also added to a PTFE vial. The acid-soluble fractions of 1 coral standard, 1 seawater standard, and all samples, as well as the 2 complete procedural blanks, were then allowed to dry inside a laminar flow chamber at 95 °C for >8 h. This protocol is adapted from that of Present et al. (Present et al., 2015, 2019).

2.3.1.3. Separation of sulfate via ion exchange chromatography. Dried samples, standards, and blanks were resuspended in 3.3 mN HCl, then transferred via micropipette to sterile Poly-Prep chromatography columns. Each column was prepared prior to the introduction of samples, standards, or blanks with a slurry of BioRad AG-1-X8 strong anion resin, 10 % HCl, and Milli-Q water, which was "rinsed" twice by the addition and elution of 3.3 N HCl, followed by Milli-Q water, then 1.6 N HNO_3, then once again by 3.3 N HCl, and finally conditioned with 0.165 N HCl and Milli-Q water. The resuspended samples, standards, and blanks were each added to their own resin-filled columns and allowed to elute for 35 min. Columns were then rinsed 3 times with Milli-Q water (i.e., water added to column and allowed to elute thrice). This eluent, which ideally contained all cations in the acid-soluble fraction of the samples and standards except sulfate, was discarded. Each column was then rinsed 3 times with 0.5 N HNO_3, to remove sulfate bound to active sites in the resin. This acidic eluent ideally contained only pure sulfate, and was captured in PTFE Savillex vials for drying inside a laminar flow chamber at 95 °C for >8 h. This protocol is adapted from those devised and refined by Paris et al. (Paris et al., 2013, 2014).

2.3.1.4. Measurement of sulfate abundance via ion chromatography. Each vial of purified sulfate was diluted with Milli-Q water to bring each to an approximate target sulfate concentration of 0–70 µM. 250 µL of each diluted sample, standard, and blank solution was aliquoted for compositional analysis via ion chromatography using a Dionex ICS-2000 in the Caltech Environmental Analysis Center, using the same method described by Johnson et al. (Johnson et al., 2021). Samples which did not yield clean sulfate peaks (i.e., contained ions other than sulfate), and/or had sulfate concentrations below the limit of detection were excluded from further analysis. 4 samples of the original 12 were thus excluded on the basis of either insufficient or unquantifiable sulfate content.

2.3.1.5. Preparation for ICP-MS. The remaining 8 samples, as well as the coral and seawater standards, and the 2 procedural blanks, were then dried for >8 h at 95 °C in a laminar flow hood. Dried samples and standards were then resuspended in a sufficient volume of 5 % HNO_3 and amended with 500 µM Na^+ solution, to bring each vial's $[SO_4^{2-}]$ to 10 µM and $[Na^+]$ to 20 µM to match the matrix of the in-house MC-ICP-MS bracketing standard (Paris et al., 2013). Procedural blanks were suspended in sufficient sodium solution in 5 % HNO_3 to have $[Na^+]$ = 20 µM. Samples, standards, and blanks were then transferred to 1.5 mL volume autosampler vials for MC-ICP-MS.

Table 1
Measured $\delta^{34}S$ of CAS, PAS, CRS, and pyrite in phosphatic and non-phosphatic microfacies of the Salitre Formation.

Sample ID*	Locality/ Section◇	Microfacies†	Target Phase‹	$\delta^{34}S$‡
Aris2_10.8	Aristeia 2	A	CAS (dolomite)	37.91 ± 0.73
Cer_23e	Cerberus	B	CAS (dolomite)	33.64 ± 0.88
FuroV_3400	CBPM Core 5	D	CAS (calcite)	29.41 ± 0.31
FuroX_3330	CBPM Core 10	C	CAS (dolomite/ calcite)	19.79 ± 0.45
FuroX_3340	CBPM Core 11	C	CAS (dolomite/ calcite)	26.59 ± 0.23
Aris1A_31.8_60.8_1	Aristeia 1	F	PAS (CFA)	30.94 ± 0.71
Aris1B_31.8_60.8_1	Aristeia 1	F	PAS (CFA)	30.94 ± 0.39
FuroX_3340_1	Aristeia 1	F	PAS (CFA)	33.42 ± 0.16
Aris_31.8_80	Aristeia 1	E	CRS (pyrite)	6.92 ± 1.06
Min_44.2	Minotaur	D	CRS (pyrite)	6.95 ± 1.29
FuroX_3330_1	CBPM Core 10	F	pyrite	23.77 ± 0.64
FuroX_3330_2	CBPM Core 10	F	pyrite	18.24 ± 0.60
FuroX_3330_3	CBPM Core 10	F	pyrite	21.78 ± 0.60
FuroX_3330_4	CBPM Core 10	F	pyrite	23.97 ± 0.60
FuroX_3330_5	CBPM Core 10	F	pyrite	33.14 ± 0.58
FuroX_3330_6	CBPM Core 10	F	pyrite	23.71 ± 0.60
FuroX_3330_7	CBPM Core 10	F	pyrite	38.47 ± 0.60
FuroX_3330_8	CBPM Core 10	F	pyrite	−1.56 ± 0.76
FuroX_3330_9	CBPM Core 10	F	pyrite/ marcasite/ pyrrhotite	−0.38 ± 0.61
FuroX_3330_10	CBPM Core 10	F	pyrite/ marcasite/ pyrrhotite	−4.24 ± 0.63
FuroX_3330_11	CBPM Core 10	F	pyrite/ marcasite/ pyrrhotite	−8.25 ± 0.71
FuroX_3330_12	CBPM Core 10	F	pyrite/ marcasite/ pyrrhotite	−7.88 ± 0.73

* Sample ID includes abbreviation for stratigraphic column and locality, as well as numbers indicating stratigraphic height and lateral distance in a measured section (both in meters) from a datum for the given column, or depth in a drill core (in cm) from the top of the core. Powders collected from the same hand samples (within centimeters of each other) are indicated with lowercase letters a-c. Note: Aris = Aristeia, Min = Minotaur, Cer = Cerberus, FuroV = CBPM Core 5, and FuroX = CBPM Core 10.

◇ Locality/Section names, stratigraphic columns, and geographic location are provided in Fig. 1.

† Microfacies A = carbonate-cemented grainstone, B = carbonate-cemented grainstone adjacent to phospatic digitate stromatolite buildup, C = carbonate-cemented grainy inter-stromatolite fill, D = carbonate-cemented laminated mudstone, E = carbonate-cemented stromatolite laminae, and F = CFA-cemented stromatolite laminae.

‹ CAS = trace structural sulfate in the lattice of the indicated carbonate mineral(s), collected via protocols for trace sulfate extraction and purification, and measured via ICP-MS. PAS = trace structural sulfate in the lattice of the indicated phosphate mineral, collected via protocols for bulk phosphate-associated sulfate extraction, and measured via EA-IRMS. CRS = chromium-reducible sulfur, extracted and fixed as Ag_2S from acid-insoluble residues, representative of sulfur in the lattice of pyrite measured via EA-IRMS. "Pyrite" and "pyrite/marcasite/pyrrhotite" refer to SIMS measurement of structural sulfur in individual crystals or aggregates of crystals.

‡ ‰ with respect to Vienna Canyon Diablo Troilite (VCDT).

2.3.2. Extraction of phosphate-associated sulfate (PAS)

Structural sulfate in carbonate fluorapatite (CFA), called phosphate-associated sulfate or PAS, is more abundant than structural sulfate in carbonate minerals, theoretically due to the similarity in size of sulfate and monophosphate anions, both of which are larger than the carbonate anion (McClellan, 1980). The more accommodating crystal structure of carbonate fluorapatite allows structural sulfate concentration in phosphorites to be 1–3 orders of magnitude greater than that of carbonate rocks (McClellan, 1980; Nathan and Nielsen, 1980), obviating the need for trace sulfate extraction protocols. Texture-specific drilling at millimeter scales generated sufficient mass of carbonate fluorapatite powders that "bulk" PAS extraction methods (Eagle et al., 2010; Stolper and Eiler, 2016) could be employed outside of a cleanroom environment.

2.3.2.1. Removal of easily soluble sulfate, organics. Because the CFA samples are all associated with organic-rich laminae in association with stromatolites, an aliquot ofeach powdered CFA sample was submerged in 3 % H_2O_2 and agitated periodically for >8 h, to oxidize any organic matter to water and oxygen. Because H_2O_2 may also oxidize sulfide minerals, resulting in leaching of trace pyrite, another aliquot of each powdered sample was treated with 1 M NaCl rinse, also for >8 h. Both the H_2O_2 and the NaCl-washed samples were then centrifuged at 13,200 rpm for 5 min, and supernate removed via micropipette. Samples were then rinsed 3 times with deionized and filtered Milli-Q water (each rinse consisting of agitation/resuspension of the powders in Milli-Q water, followed by centrifuging, and removal of supernate).

2.3.2.2. Carbonate mineral leaching. Carbonate minerals (calcite and dolomite) were removed from the powders by acetic acid leaching. Washed powders were suspended in 0.1 M acetic acid and agitated continuously for 36 h at ambient lab temperatures (~25 °C). Afterward, powders were resuspended using a mini-vortexer, centrifuged for 5 min at 13,200 rpm, and the supernate discarded. Again, samples rinsed 3 times with deionized and filtered Milli-Q water (each rinse consisting agitation/resuspension of the powders in Milli-Q water, followed by centrifuging, and removal of supernate). Leached and rinsed samples were then dried at 65 °C for >8 h.

2.3.2.3. Acid digestion of carbonate fluorapatite. Dried CFA powders, cleaned of easily soluble sulfate, organic material, and carbonate minerals, were placed in 2 N HCl and allowed to react at 25 °C for >8 h. The acidic leachate (pH = 2) was then filtered through 0.05 µm nitrocellulose filter paper and allowed to react at ambient lab temperatures (~25 °C) with 5 % $BaCl_2$ for >8 h. Acid-insoluble residues (collected on filter paper) were stored and dried at 60 °C for >8 h before being scraped with an aluminum spatula into microcentrifuge tubes for extraction of chromium-reducible sulfur.

2.3.3. Extraction of chromium-reducible sulfur (CRS)

2.3.3.1. Modified reduced sulfur extraction protocol. Acid insoluble residues, collected after the acid digestion by 2 N HCl of carbonate and CFA sample powders as described above, were rinsed three times with Milli-Q water, collected on 0.05-µm nitrocellulose filter paper, dried, and weighed. For each sample, between 5 and 500 mg of dried acid-insoluble residue was added to an acid-washed, triple-necked glass reaction vessel, along with a small (<1 mL) volume of EtOH to prevent static cling of dry sample to reaction vessel wall. Reaction vessels were placed in a heating nest and warmed. To each reaction vessel, we attached (1) a valve-controlled connection to a continuous flow of N_2 gas, (2) a cannula allowing for the introduction of liquid reagents, and (3) a cold water

condenser attached to a gas-escape tube which was submerged in a "sulfide trap" solution of 10 % NH_4OH and 3 % Zn-acetate. Through cannula (2), we gradually introduced the following reagents to each reaction vessel: 10 mL of 12 N HCl and 20 mL of a chromium reduction solution (~2 M $Cr(III)Cl_3{\cdot}6H_2O$ in 0.5 N HCl solution, passed through a column packed with Zn pellets - amalgamated from powder via reaction with mercuric nitrate - under vacuum). Chromium-reducible sulfur was released from the dissolving powders as gaseous H_2S, separated from water vapor during passage through the cold-water condenser on reaction vessel neck (3) and bubbled through the trap solution of NH_4OH and Zn-acetate. In this basic trap solution, H_2S is converted to HS^- and S_2, which react with zinc ions in solution to yield ZnS. A small aliquot of ZnS in trap solution from each sample was extracted and measured via colorimetric assay to ascertain sulfide abundance. The remaining ZnS in trap solution was treated with $AgNO_3$ solution to fix sulfide as solid Ag_2S for combustion to SO_2 and measurement via EA-IRMS.

2.3.3.2. Colorimetric assay for sulfide abundance. Abundance of sulfide in solution is commonly measured through a modified version of the Cline Assay (Cline, 1969), wherein solutions in which sulfide species have been fixed as ZnS are reacted with Cline Reagent, a mixture of N,N-dimethyl-p-phenylenediamine sulfate and hydrated ferric chloride dissolved in 50 % HCl. The colored complex formed between ZnS and diamine and Fe^{3+} has a maximum absorbance at $\lambda = 670$ µm, and the intensity of this absorbance scales directly with ZnS abundance in the treated solution. Aliquots of trap solution for each sample were serially diluted with Milli-Q water alongside a range of standards of known ZnS concentration in 96-well acrylic plates. These were each treated with the Cline Reagent, allowed to react for ~2 h, and their absorbance at $\lambda = 670$ µm, measured using a plate-reading spectrophotometer. The absorbances of a range of standards of known ZnS concentration were used to calibrate the relationship between absorbance and [ZnS], which was then applied to the samples of unknown concentration.

2.3.4. Identification of primary or early diagenetic pyrite crystals (PYR), individual and aggregate

Fe-sulfide crystals — putative pyrites — were identified by their opacity under transmitted white light and their brassy yellow, metallic sheen under reflected white light using optical petrographic microscopy on samples prepared as 30-µm-thick thin sections. The relative timing of their growth (authigenic, early diagenetic) was determined via cross-cutting relationships and spatial association with early cement phases and amorphous organic material, as opposed to late-stage, fracture-filling cements (Sanders and Grotzinger, 2021; Sanders et al., 2023). Crystals and crystal aggregates selected for analysis via Secondary Ion Mass Spectrometry (SIMS) had a cross-sectional diameter of ~20 µm; e.g., Fig. 4.

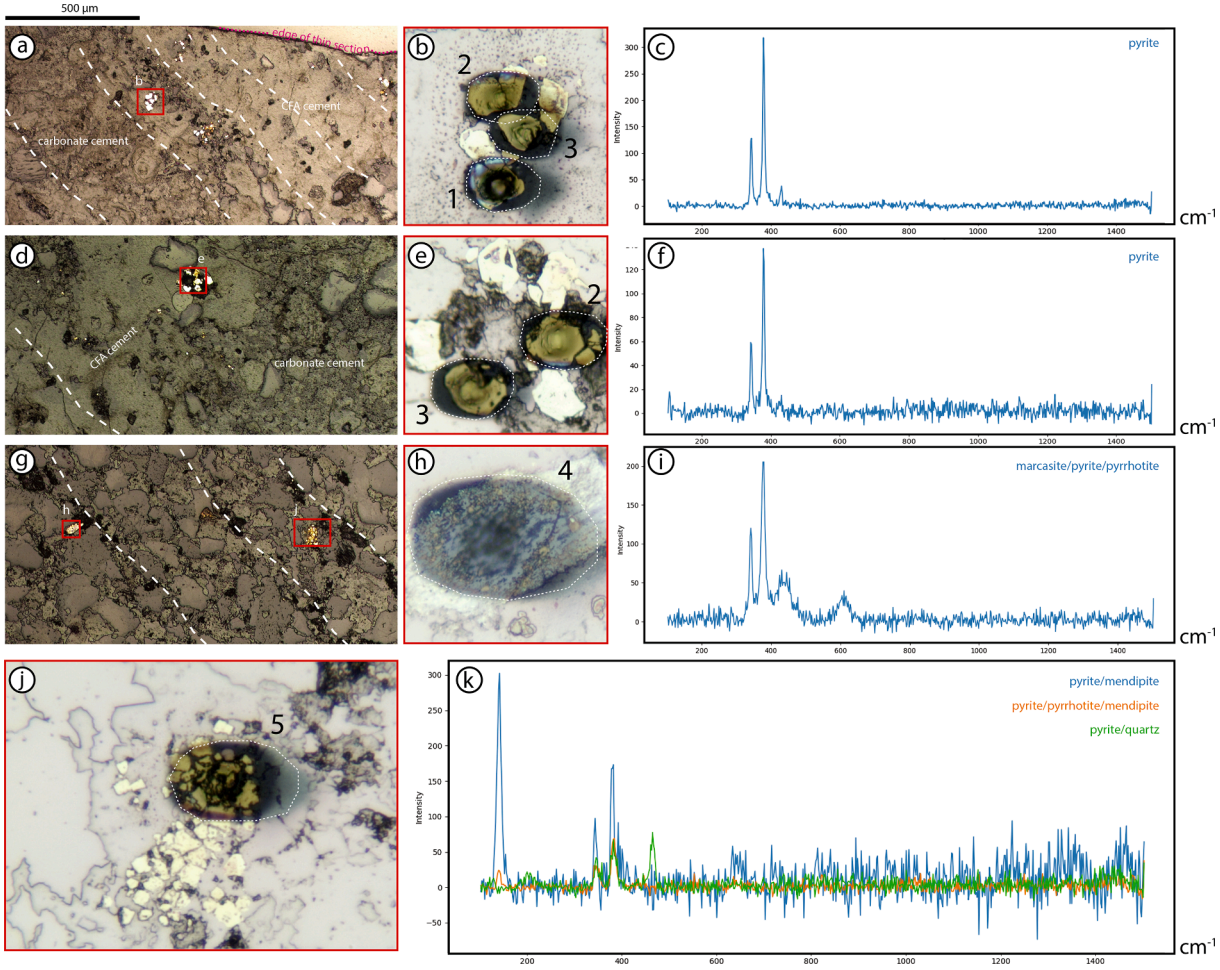

Fig. 4. Reflected light photomicrographs and Raman spectra of a representative subset of individual and aggregate Fe-sulfide crystals in thin section, whose $\delta^{34}S$ compositions were measured via SIMS. (a, d, and g) Annotated photomicrographs of target crystals in their microfacies context. (b, e, h, and j) Magnified insets of crystals and crystal aggregates. Dotted white lines demarcate the area sputtered by the primary ion beam, and numbers indicate the order in which measurements were made in each pictured area. (c,f,i, and k) Raman spectra collected from crystals within the sputtered areas, and the mineralogies with which they are associated.

2.4. Sulfur Isotope Measurements

Sulfur isotope composition (d34S) of structural sulfur in selected mineral phases were measured by 3 different methods, described in this section and summarized in Fig. S1. Also described are the criteria for inclusion or removal of specific data from the analytical pipeline and further discussion and interpretation (See Fig. S2).

2.4.1. MC-ICP-MS

2.4.1.1. Collection of isotopic data. The $\delta^{34}S$ values of structural sulfate extracted from carbonate mineral samples (CAS) were measured via Thermo Fisher Scientific Neptune Plus multicollector inductively-coupled plasma-source mass spectrometry (MC-ICP-MS) with a Cetac Aridus II desolvating spray chamber following methods of Paris et al. (Paris et al., 2013). Autosampler vials containing 8 carbonate samples' extracted trace sulfate as sodium sulfate in HNO_3 solution were measured alongside vials containing trace sulfate from 1 seawater standard, 1 coral standard, and 2 procedural blanks — each vial's contents being measured twice. Each measurement was bracketed by the measurement of a laboratory reference sodium sulfate solution of known isotopic composition.

2.4.1.2. Reduction of isotopic data. Each set of 50 acquisition cycles for each intermediate replicate of samples, standards, and procedural blanks were monitored for any time-dependent trends in intensity (i.e., correlations between measured mass ratio $^{34}R/^{32}R$ and acquisition number). Drift in the instrument's ionization efficiency and detector response to ion flux over time is expected, and may be quantified and corrected for using bracketing laboratory standard solution. However, significant drift on timescales smaller than the acquisition time of a single sample are indicative of instrumental effects that cannot be well-quantified, and measurements whose accuracy and precision cannot be well-constrained. 1 replicate measurement of sample *Aris_10.8* was excluded from further analysis by this metric, as well as 1 replicate measurement of *Min_26.4*.

Procedural blanks provided a constraint for the isotopic composition and abundance of background sulfate. Sulfate abundance in the 2 procedural blanks (4 total measurements) was: 1.37 nmol and 0.40 nmol total, with $\delta^{34}S$ of 13.58 ± 0.08 ‰ (VCDT) and 4.06 ± 0.23 ‰ (VCDT), respectively. Isotope mass ratios for all samples and standards were corrected for this background sulfate. Depending on the sulfate mass in each sample, this correction affected $\delta^{34}S$ values by + 0.004 to 1.1 ‰, less than the standard error of the population of 50 acquisition cycles which described the precision of each measurement.

Measurement of the seawater standard and the coral standard provided a metric of accuracy for corrected $\delta^{34}S$ values of unknown samples. After correction for background sulfate constrained by the procedural blanks, $\delta^{34}S$ of the coral standard was 22.68 ± 0.18 ‰ (VCDT). For the seawater standard, blank-corrected $\delta^{34}S$ was 21.05 ± 0.19 ‰ (VCDT). These values are within one standard error of the accepted $\delta^{34}S$ values for these standard materials (Paris et al., 2013).

Relative intensity (RI) of the signal from each sample measurement compared to the signal from bracketing laboratory reference measurements was monitored throughout. RI values near 1.0 indicate that the amount of sulfate in the sample is close to the amount of sulfate in the laboratory standard, and therefore should have similar mass bias. RI values between 0.9 and 1.1 reflect samples whose mass bias — related to mismatching of the sample matrix with that of the in-house bracketing standard — is less than analytical precision (Paris et al., 2013). 3 samples with RI values outside of this range were excluded from further analysis due to poor matrix-matching. Poor matrix matching can result in inaccurate $\delta^{34}S$ data, and may indicate potentially incomplete sulfate purification during anion exchange chromatography. These 3 samples were all from the same locality and collected from within the same stratigraphic section, and indeed all 3 yielded significant amounts of acid-insoluble residue during the sample preparation and cleaning process - suggesting that these samples may have had high abundance of unquantified contaminants, possibly kerogenous material.

$\Delta^{33}S$ expresses the difference between measured $\delta^{33}S$ of a sample, standard, or reference material, and the $\delta^{33}S$ expected based on mass-dependent fractionation of ^{32}S, ^{33}S, and ^{34}S. As no mass-independent fraction of ^{33}S is expected in these Neoproterozoic samples, $\Delta^{33}S$ values differing from 0 ‰ by magnitudes greater than calculated analytical errors were considered a metric of plasma interferences and contamination of signal by ions other than sulfur. Thus, measurements of samples with $\Delta^{33}S$ outside the range −1.5 to 1.5 ‰ were excluded from further analysis. 2 samples would have been excluded by this metric, but had already been culled from the dataset on the basis of unacceptably large relative intensities consistent with ineffective sulfate purification by anion exchange chromatography.

Ultimately, 5 of the original 12 samples yielded $\delta^{34}S$ of CAS for which precision and accuracy were considered reliable.

2.4.2. EA-IRMS

2.4.2.1. Collection of isotopic data. The $\delta^{34}S$ values of structural sulfate extracted from CFA-cemented samples (PAS) and of chromium-reducible sulfide (CRS) were measured via a combined Thermo Elemental Analyzer and Thermo Delta Plus XL isotope ratio mass spectrometer (EA-IRMS). Samples of PAS fixed as dried $BaSO_4$ powders and samples of CRS fixed as Ag_2S powders, as well as Ag_2S standards with a range of known isotopic composition, were weighed into tin foil capsules, each containing between 4 and 5 μg sulfur, which were sealed and compressed to remove air. These were loaded into the elemental analyzer, undergoing combustion with O_2 gas, such that sulfur in $BaSO_4$ and Ag_2S was converted to SO_2. SO_2 gas was passed through a network of solid and gaseous reagents which ensured its redox state, then a chromatographic column and water trap to remove non-SO_2 contaminants which may have volatilized during the combustion process, then into the ion source and analytical path of the isotope ratio mass spectrometer. A series of automated valves alternated the stream of the SO_2 gas from combusted samples and standards with aliquots from a reservoir of laboratory reference SO_2 gas of known isotopic composition. Each measurement consisted of repeated cycles of reference gas and analyte gas via magnetic sector isotope ratio mass spectrometry, wherein Faraday cups attached to amplifiers measured the flux of ions of $m/z = 64$ and 66, allowing for the calculation of the mass ratio $^{34}R/^{32}R$ and thereby $\delta^{34}S$ of PAS, CRS, and sulfur isotope standards.

2.4.2.2. Reduction of isotopic data. All measurements of samples and standards were corrected for instrumental drift with respect to ionization efficiency, detector response, and other sources of non-linearity between isotopic composition of a gas and measured composition, by monitoring $^{34}R/^{32}R$ of laboratory standard SO_2 gas over the course analysis.

Measurements of sets of 10 samples of unknown isotopic composition were bracketed by 2 sets of measurements of at least 6 standards of known isotopic composition (i.e., paired replicates of 3 different standard materials). Least-squares linear regression was performed to describe the linear relationship between standards' measured $\delta^{34}S$ and their known/accepted $\delta^{34}S$ values. Each sample's measured $\delta^{34}S$ value was converted into the reference frame established by the bracketing standards by applying the linear relationship between measured-and-accepted values from the preceding set of standards as well as the linear relationship from the succeeding set of standards, and taking the average of the two converted values.

2.4.3. 7f-GEO-SIMS

2.4.3.1. Collection of isotopic data. Samples for which the yield of chromium reducible sulfur (CRS) extraction was less than the analytical limit of EA-IRMS (~4 μg S), but in which intergrowth of pyrite with CFA cements was still observable via petrographic thin section, were identified as targets for analysis using the Caltech Microanalysis Center's Cameca IMS 7f-GEO Secondary Ion Mass Spectrometer (SIMS). Individual pyrite crystals or aggregates of crystals with diameters ≥20 μm were identified using reflected light microscopy.

Petrographic thin sections containing target pyrite crystals, 30 μm thick, were sputter-coated with gold, negatively charged via electron gun, then bombarded with a pulsed primary ion beam of Cs^+ cations which, at the voltages employed, had a beam width of roughly 20 μm. The energetic primary Cs^+ ions generated by the 7f-GEO SIMS ion source displace and liberate a cascade of secondary ions from a small analytical volume within the target crystals. These secondary ions enter a magnetic sector mass spectrometer via a series of ion optics. Faraday cup detectors equipped with amplifiers measured flux of secondary ions of $m/z = 32$, 33, and 34 (sulfur) as well as 16 (oxygen). These ion fluxes were used to calculate $^{34}R/^{32}R$ and thus $\delta^{34}S$ of the structural sulfur of the interrogated pyrite crystals.

2.4.3.2. Reduction of isotopic data. Each measurement consisted of 29–30 acquisitions of secondary ion flux from the same pyrite crystal. Measurements of target pyrite crystals of unknown composition were bracketed by repeated measurements of an in-house pyrite standard. Replicate standard measurements were used to quantify the relationship between signal/instrument response and actual sulfur isotopic composition of the sample, capturing any fractionation between the analyte and the population of secondary ions generated. The standard error of $\delta^{34}S$ values measured for the bracketing standards was propagated with standard error of the population of 29–30 acquisitions for each measurement of a pyrite crystal of unknown composition, to quantify the measurements' precision (0.6–0.7 ‰).

3. Results

Here, we present $\delta^{34}S$ values of (1) structural sulfate in the mineral lattice of dolomite and calcite cements, or carbonate-associated sulfate (CAS), (2) structural sulfate in the mineral lattice of carbonate fluorapatite cements, or phosphate-associated sulfate (PAS), and (3) sulfide in the mineral lattice of pyrite crystals (FeS_2). CAS is a trace chemical component of carbonate rock, having concentrations of ppt to ppm in most natural samples, and ideally represents a subsample of the aqueous sulfate in the fluids from which the carbonate rock precipitated. PAS is more abundant than CAS per unit mass of the host mineral, with concentrations of order 10–100 ppm. The sulfate incorporated into the structure of these cement-forming minerals ideally are an isotopically representative subset of the aqueous SO_4^{2-} in the fluids from which the cements precipitated. Likewise, sulfide in pyrite is derived from the aqueous H_2S and S^{2-} in the parent solution from which the pyrite grew. Thus, paired measurements of $\delta^{34}S$ of CAS/PAS and $\delta^{34}S$ of pyrite in rocks that were deposited and cemented at the same time and place provide a snapshot of the difference in isotopic composition of oxidized and reduced sulfur species in the same pore fluid.

We interrogate two distinct textural classifications: carbonate-cemented and phosphate-cemented. The carbonate-cemented class includes laminated and/or cross-stratified carbonate grainstones, mudstones, and boundstones (stromatolite buildups), comprised of carbonate grains in carbonate cements. The phosphate-cemented class includes stromatolitic laminae in boundstone/mudstone, comprised of carbonate micrite and grains in cryptocrystalline carbonate fluorapatite cement. Abundance of CAS and pyrite and paired $\delta^{34}S$ measurements of CAS and pyrite in carbonate-cemented facies should - theoretically - provide a constraint on sulfur cycling in the pore waters in which carbonate mineralization was favored. Abundance of PAS and pyrite and paired $\delta^{34}S$ measurements of PAS and pyrite in phosphate-cemented facies should provide a constraint on sulfur cycling in phosphate-mineralizing pore waters. These data are described below and summarized in Table 1 and Fig. 5.

3.1. Abundance and $\delta^{34}S$ of CAS and Fe-sulfides in carbonate-cemented textures

The weight percent of sulfate in the carbonate-cemented samples analyzed here was calculated from the molar concentration of SO_4^{2-} in the purified, acid-soluble fraction of each powdered and cleaned sample of mm-scale drill tailings (as measured by ion chromatography) relative to the original mass of the powder sample - see Methods. Samples which had sulfate concentrations above the detection limit of the ion chromatograph, sufficient to aerosolize and convert to an ionized beam for ICP-MS, had concentrations of 7–42 ppm. Carbonate samples at the lower end of this range included *Cer_23e* ([CAS] = 7.3 ppm) and *Aris2_10.8* ([CAS] = 12 ppm), which are taken from cross-stratified oolitic grainstone facies characterized in the *Cerberus* and *Aristeia* localities, respectively. In the case of *Cer_23e*, the sampled grainstone was immediately adjacent to (i.e., within a few lateral centimeters of) CFA-cemented digitate stromatolites and represent carbonate sedimentation at the same time interval and depositional setting as the cementation of the stromatolites. Carbonate samples at the higher end of the observed range of CAS abundances included *FuroX_3330* and *FuroX_3340* (which sample the carbonate grainstone immediately adjacent to CFA-cemented digitate and disordered stromatolite facies in *CBPM Core 10,* with [CAS] of 30 ppm and 31 ppm, respectively), and *FuroV_3400* (which sampled very fine planar-to-crinkly-laminated carbonate mudstone in *CBPM Core 5*, with [CAS] of 42 ppm).

The $\delta^{34}S$ value of CAS ($\delta^{34}S_{CAS}$) in the 5 above-described samples represents sulfur isotope composition of an admixture of the of the structural sulfate in micritic and interlocking anhedral mosaic cements of calcite and/or dolomite, with minor contributions from the micritized peloids and ooids suspended in those cements. Procedures to remove easily soluble sulfate phases outside of the carbonate mineral lattice, and from oxidized sulfide minerals, should minimize the contributions of these other phases to the measured samples. Carbonate grainstone facies immediately adjacent to CFA-cemented stromatolite facies yielded $\delta^{34}S_{CAS}$ of 33.64 ± 0.88 ‰VCDT (*Cer_23e*), 19.79 ± 0.45 ‰VCDT (*FuroX_3330*), and 26.59 ± 0.23 ‰VCDT (*FuroX_3340*), where errors represent ± 1 standard error around the mean of a population of 50 acquisition cycles for a given sample. Carbonate grainstone facies not associated with stromatolites yielded $\delta^{34}S_{CAS}$ of 37.91 ± 0.73 ‰VCDT (*Aris2_10.8*). Carbonate mudstone facies not associated with stromatolites yielded $\delta^{34}S_{CAS}$ of 29.41 ± 0.0.32 ‰VCDT (*FuroV_3400*).

Pyrite crystals which cross-cut or are intergrown with micritic and interlocking anhedral mosaic carbonate cements represent an extremely minor component in the carbonate-cemented rocks of the Salitre Formation. Structural sulfur in this pyrite was extracted as CRS. Cline Assay of CRS fixed as ZnS provided a minimum constraint on the abundance of CRS in the measured samples *Aris_31.8_80* and *Min_44.2*: <10 ppm S in each. Note: concentrations are calculated via the measured concentration of CRS in an aliquot of the rinsed, dried, acid-insoluble residue after washing and HCl-leaching of carbonate samples (described in Methods), and represent the sulfide extracted from the mineral pyrite (FeS_2), but *not* from other sulfide pools such as pyrrhotite (FeS) or organically-bound sulfide.

The $\delta^{34}S$ values of CRS ($\delta^{34}S_{CRS}$) in our three carbonate-cemented samples which had abundances above the threshold of our analyses (See Methods), represent the sulfur isotope composition of the reduced H_2S or S^{2-} which was captured by reaction with reduced iron (Fe^{2+}) during and subsequent to cementation/lithification. Our sampling method, which avoided veins and close spatial associations with late-

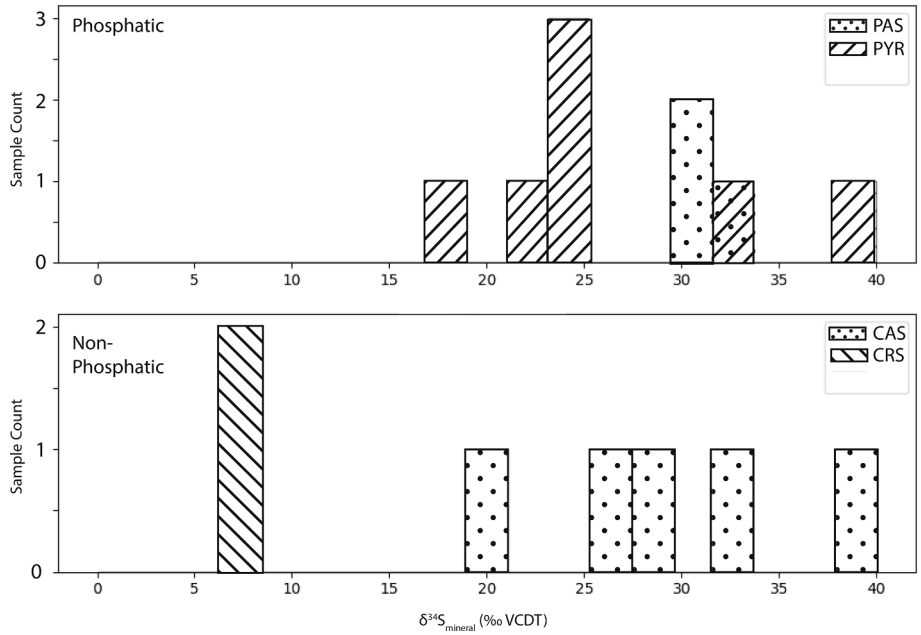

Fig. 5. Histogram of $\delta^{34}S_{mineral}$ values. PAS = $\delta^{34}S$ of phosphate-associated sulfate, i.e. structural sulfate in carbonate fluorapatite (CFA), measured via EA-IRMS. CAS = $\delta^{34}S$ of structural sulfate in calcite and dolomite, measured via ICP-MS. PYR = $\delta^{34}S$ of structural sulfide in pyrite, measured via SIMS. CRS = $\delta^{34}S$ of chromium-reducible sulfide, measured via EA-IRMS. Upper plot contains values from phosphatic facies. Lower plot contains values from non-phosphatic, carbonate-cemented facies.

stage diagenetic phases, should have minimized the contribution to CRS from sulfide associated with diagenetic fluids after deep burial, such that the measurements may be considered a proxy for sulfide scavenged by trace Fe^{2+} in anoxic to suboxic sediment pore waters (early diagenesis). Pyrite S extracted as CRS, associated with carbonate-cemented stromatolite laminae, yielded $\delta^{34}S_{CRS}$ of 6.92 ± 1.06 ‰VCDT (average and standard error of 2 replicates of *Aris_31.8_80)*. Pyrite S extracted as CRS, associated with carbonate-cemented cross-stratified grainstone, yielded $\delta^{34}S_{CRS}$ of 6.95 ± 1.29 ‰VCDT (average and standard error of 2 replicates of *Min_44.2)*.

3.2. Abundance and $\delta^{34}S$ of PAS and Fe-sulfides in phosphate-cemented textures

The abundance of structural sulfate in carbonate fluorapatite cement samples (PAS) could only be given a minimum constraint, based on the mass yield of $BaSO_4$ from $BaCl_2$ reaction with decarbonated, acid-soluble filtrates derived from purified powders of carbonate fluorapatite - see Methods. ~500 mg of cleaned and purified CFA powder yielded ~5 mg of $BaSO_4$ (0.192 mg -SO_4), implying PAS concentration in the measured samples of at least 384 ppm.

The $\delta^{34}S$ value of structural sulfate in carbonate fluorapatite cements ($\delta^{34}S_{PAS}$) represents sulfur isotope composition of the aqueous sulfate in the pore waters from which the cements precipitated. There were only a few samples suitable for this analysis (i.e., extracted from well-characterized fabrics and having sufficiently high PAS concentrations to allow for bulk rather than trace sulfate extraction methods). These included: *Aris1A_31.8_60.8*, *Aris1B_31.8_60.8*, and *FuroX_3340*, from digitate stromatolite buildups in the *Aristeia* locality and *CBPM Core 10*. A set of 3 replicate measurements of the sulfur isotope composition for PAS in *Aris1A_31.8_60.8* yielded values of $\delta^{34}S_{PAS}$ = 30.94 ± 0.71 ‰ VCDT. 3 replicate measurements for PAS in *Aris1B_31.8_60.8* yielded $\delta^{34}S_{PAS}$ = 30.94 ± 0.39 ‰VCDT. 3 replicate measurements for PAS in *FuroX_3340* yielded $\delta^{34}S_{PAS}$ = 33.42 ± 0.16 ‰VCDT. (Note: confidence intervals are given as the standard error.).

Sulfide minerals that were intergrown with or appeared to cross-cut cryptocrystalline carbonate fluorapatite cements were in low abundance, and their structural sulfide could not be extracted as CRS from the small quantities of powder that result from mm-scale drilling of specific textures. Individual pyrite crystals and aggregates of crystals within the relevant textures and larger than the Cs^+ beam of the 7f-GEO-SIMS at a given current (here, ≥ 20 μm) were thus selected for SIMS analysis, but total abundance and bulk isotopic composition of phosphate-associated pyrite was not measured.

The $\delta^{34}S$ value of pyrite associated with carbonate fluorapatite-cemented textures ($\delta^{34}S_{pyr}$), as in the carbonate-cemented facies, represent the sulfur isotope composition of the reduced H_2S or S^{2-} which was captured by reaction with reduced iron (Fe^{2+}) during and subsequent to cement precipitation from sediment pore waters. The mineral pyrite (FeS_2) may form by the reaction of Fe^{2+} and sulfide ions in solution, but so can other phases such as marcasite (also FeS_2), or troilite/pyrrhotite (FeS). Pyrite is one of the more stable iron sulfide phases in the temperature and pressure regimes of the crust's upper few kilometers, and so may represent the primary phase in which sulfide was mineralized or recrystallized pseudomorphs after less stable or less oxidized iron sulfide minerals. Measuring the isotopic composition of iron sulfide minerals via SIMS allows for the analysis of individual and aggregate crystals of iron sulfide phases whose mineralogies have been independently confirmed by other methods to be pyrite, and which are not spatially associated with later-stage diagenetic features. However, we did analyze some iron sulfide crystal aggregates which may have integrated the secondary ions generated by sputtering of not only pyrite, but other closely associated minor iron-sulfide phases, namely marcasite and pyrrhotite (Fig. 4). Such secondary ions would not have been generated according to the same physics as the interaction of the primary ion beam with the pyrite standard, and so the $\delta^{34}S$ measured on less-than-pure-pyrite SIMS targets (henceforth, $\delta^{34}S_{pyr,mix}$) would likely be inaccurate (Riciputi et al., 1998; Kozdon et al., 2010; Kita et al., 2011).

$\delta^{34}S_{pyr}$ of confirmed pyrite crystals ≥ 20 μm in diameter and associated with carbonate-fluorapatite-cemented textures were successfully measured via SIMS in only one well-characterized sample: *FuroX_3330*, a sample from phosphatic digitate stromatolite facies within *CBPM Core 10*. $\delta^{34}S_{pyr}$ values in this sample were: 23.77 ± 0.64 ‰VCDT, 18.24 ±

0.60 ‰VCDT, 21.79 ± 0.60 ‰VCDT, 23.97 ± 0.60 ‰VCDT, 33.14 ± 0.58 ‰VCDT, 23.71 ± 0.60 ‰VCDT, and 38.47 ± 0.60 ‰VCDT, where errors are the standard error of a set of 50 measurements of a continuously generated secondary ion beam, corrected for instrumental response according to parallel measurements of a pyrite standard of known composition (see Methods). This wide range of values (~18 to 38 ‰VCDT) were retrieved for pure pyrite crystals in the same sample, and from at the same position in the paragenetic sequence of that sample — reflecting either a wide range in pore water sulfide compositions at the time of their formation (due to micro-scale variations in aqueous chemistry in pores under conditions of limited pore connectivity) or a wide range in the timing of each crystal's formation with respect to sulfur cycling in the porespace.

A population of possible admixtures of pyrite with other iron-sulfide minerals including pyrrhotite and marcasite was measured as well (see Fig. 4g, j, and k), yielding $\delta^{34}S_{pyr,mix}$ of −1.56 ± 0.76 ‰VCDT, −0.38 ± 0.61 ‰VCDT, −4.24 ± 0.63 ‰VCDT, −8.25 ± 0.71 ‰VCDT, and −7.88 ± 0.73 ‰VCDT. These values may reflect reduced-iron capture of isotopically lighter sulfide introduced to the sedimentary rock by a different generation of pore fluids, but the difference in matrix effects on secondary ion beam production between pure pyrite and possible mixtures of pyrite and other iron-sulfide phases cannot here be constrained, and so these measured values are excluded from the discussion below.

4. Discussion

In this study, we measured $\delta^{34}S$ of structural sulfate in samples of carbonate (calcite) and phosphate (CFA) cements and $\delta^{34}S$ of pyrite sulfide from the Ediacaran Salitre Formation in Eastern Brazil. Petrographic thin sections and cut surfaces corresponding to the samples discussed herein were previously analyzed via SEM/EDS, Raman spectroscopy, and XRF mapping in a study which determined that the targeted sulfate- and sulfide-bearing phases and were likely synformational and derived from the same fluids (Sanders and Grotzinger, 2021; Sanders et al., 2023). Measurements of the sulfur isotope composition of oxidized and reduced sulfur in synformational mineral phases may be used to constrain the nature of biogeochemical sulfur cycling in the fluids from which cement phases precipitated (Shields et al., 2004; Fike and Grotzinger, 2008; Wotte et al., 2012). Here, we compare the sulfur isotope composition of oxidized and reduced sulfur species in phosphatic and non-phosphatic facies of the Salitre Fm. to determine whether there may have been systematic differences in biogeochemical sulfur cycling correlated with early phosphogenesis.

4.1. Framework for the interpretation of $\delta^{34}S_{SO4}$, $\delta^{34}S_{sulfide}$, and $\Delta^{34}S$ in phosphatic- and non-phosphatic cemented fabrics

As earlier stated, the isotopic composition of sulfur incorporated into early-forming pore cements as structural sulfate and as minor pyrite represent the net effect of many different sulfur reactions occurring in pore fluids. The importance of these reactions (i.e., the proportion of the pore fluid sulfur on which they act), and the kinetic fractionation effects with which they are associated, are many and varied. Furthermore, mineralization of CFA and carbonate cements with trace sulfate, and mineralization of sulfide as pyrite, may have occurred at any point in the progress of sulfate- and sulfide-involved reactions - such that the $\delta^{34}S$ of sulfate in co-occurring cements, or of sulfide in intergrown pyrite crystals, may represent pore water sulfate and sulfide in different moments of isotopic disequilibrium.

It may not be possible to deconvolve all of the reactions effecting sulfur isotopic composition of sulfate and sulfide based on the "snapshots" provided by the $\delta^{34}S$ of sulfur in structural sulfate and sulfide in co-occurring mineral phases. However, it may be possible to constrain the likelihood that certain reactions were prevalent in pore fluids at the time of cementation. Significant differences between CFA and carbonate-cemented textures with respect to $\delta^{34}S_{SO4}$, $\delta^{34}S_{sulfide}$, and the quantity $\Delta^{34}S = \delta^{34}S_{SO4} - \delta^{34}S_{sulfide}$ may provide clues to differences in microbial metabolic activity which determined the spatial distribution of sedimentary phosphorite. Biological and abiological components of the pore fluid chemistry which may impact the sulfur isotope composition of early-forming cement phases include: sulfate concentrations of the seawater from which pore fluids were derived, as well as the relative rates and kinetic isotope effects of microbial sulfate reduction, sulfide oxidation, and sulfur disproportionation occurring in pore fluids at different depths below the sediment–seawater interface. If starting seawater sulfate concentrations are low - as may be the case in some Ediacaran basins (Halverson and Hurtgen, 2007; Ries et al., 2009; Loyd et al., 2012; Laakso et al., 2020) — or there is limited communication between pore fluids and the wider ocean, isotopic fractionation might be small between sulfide derived from microbial sulfate reduction and the starting sulfate pool due to fractionation effects in a closed system. Conversely, when sulfate is readily available, the fractionation effect of microbial sulfate reduction may be large; and recorded in the $\Delta^{34}S$ between structural sulfate and sulfide in pore fluid-derived cements. In this case, one may expect $\Delta^{34}S$ between cement-associated sulfate and pyrite sulfide to be on the order of ~15–30 ‰ or even more, when microbial sulfate reduction is prevalent in pore waters (Harrison and Thode, 1958; Boudreau and Westrich, 1984; Habicht and Canfield, 2001; Brunner and Bernasconi, 2005; Canfield et al., 2010; Bradley et al., 2016; Gomes and Johnston, 2017).Sulfur disproportionating microorganisms are also capable of producing large fractionations between sulfate and sulfide pools. The light isotopologue of SO_4^{2-} is preferentially taken up by these microorganisms, and then preferentially reduced to SO_3^{2-} (sulfite), $S_2O_3^{2-}$ (thiosulfate), and S_0 and other intermediate sulfur species. Light isotopologues of these intermediates are then preferentially reduced to sulfide. The sulfide pool produced by reduction of sulfur intermediates is thus more ^{34}S-depleted relative to the starting sulfate pool than if only direct sulfate reduction had taken place, which may result in $\Delta^{34}S$ of 40–70 ‰ (Habicht et al., 1998; Habicht and Canfield, 2001; Farquhar et al., 2003; Lesniak et al., 2003; Hurtgen et al., 2005; Johnston et al., 2005).

Thus, both microbial sulfate reduction and sulfur disproportionation can generate a ^{34}S-enriched pool of pore fluid sulfate and a ^{34}S-depleted pool of pore fluid sulfide under conditions where pore fluids are derived from seawater with abundant sulfate (i.e., relatively oxidizing).

If microbial sulfide oxidation to sulfate is prevalent in sediments, there may be a significant contribution to the pore water sulfate pool of ^{34}S-depleted sulfate - since the H_2S utilized by sulfide-oxidizing microorganisms is the direct metabolic product of microbial sulfate reduction (MSR). This could result in similar $\delta^{34}S$ values for sulfate and sulfide, i.e. $\Delta^{34}S \approx 0$ ‰ (Dale et al., 2009; Arning et al., 2009; Gomes and Johnston, 2017). In addition, the kinetic fractionation effects of microbial sulfide oxidation may result in several-per-mil ^{34}S-enrichment of the sulfide pool ($\Delta^{34}S = -5$–0 ‰), depending on the biochemical pathways utilized and whether ancient sulfide-oxidizing microorganisms utilized O_2 and NO_3^- like their counterparts in modern phosphogenetic environments (Kaplan and Rafter, 1958; Poser et al., 2014). Interestingly, it is also possible for some sulfide-oxidizing microorganisms to disproportionate the S_0 intermediate, resulting in highly ^{34}S-enriched sulfate - producing $\Delta^{34}S$ comparable to microbial sulfate reduction (Pellerin et al., 2019).

Another factor which may result in differences in $\delta^{34}S$ between different cement phases is the evolution of the chemical and isotopic character of the same pore volume as it is buried successively deeper below the sediment–water interface. Concentration gradients of various ions may be steep over mere millimeters of depth below the sediment–water interface, and so apparently "synformational" cements may capture different pore fluid chemistries, recording the effects of progressive distillation and the restriction of diffusive transport as much as microbial metabolic machinery.

4.1.1. A Note on direct comparison/pairing of sulfate and sulfide $\delta^{34}S$ in different samples

Ideally, one would only directly compare the isotopic compositions of sulfate and sulfide-bearing phases which precipitated from the same pore volume, in order to confidently derive information about the influence of various metabolic processes on the same sulfur pool. Unfortunately, in this study, it was not possible to collect sufficient masses of sulfur-bearing material for $\delta^{34}S$ measurements of PAS, CAS, and PYR/CRS all from the same mm-scale cement pockets — nor was it possible to determine how connected individual pore volumes may have been at the time of cement precipitation. Nevertheless, it is not unreasonable to suppose that similar processes were occurring in pore volumes which generated similar cement fabrics and occurred within the same depositional facies. Thus, we consider it reasonable to compare sulfur isotope composition of sulfate and sulfide-bearing phases which precipitated in different pore volumes — provided that those phases are associated with the same depositional facies and the same or similar stratigraphic heights, and that there is no textural or isotopic evidence of significantly different diagenetic histories. The difference ($\Delta^{34}S$) between $\delta^{34}S_{SO4}$ and $\delta^{34}S_{sulfide}$ of these phases can still provide a constraint on sulfur isotope systematics in carbonate-precipitating pore fluids of the Salitre Formation. The annotated stratigraphic columns in Fig. 2 indicate the stratigraphic levels and lithofacies associations of all of the samples included in Table 1, Fig. 5, and Results and Discussion; associations which are further explicated in previous publications (Sanders and Grotzinger, 2021; Sanders et al., 2023). We directly compare the isotopic composition of samples with similar/identical paragenetic histories and lithofacies associations, collected from within millimeters to meters of one another, despite the fact that those phases did not necessarily precipitate from the same pore volumes.

4.1.2. A note on direct comparison of $\delta^{34}S$ values obtained by different methodologies

We believe that, to the extent of our analytical capacities, the measured values do reflect the actual isotopic compositions of the target cement phases, and our methods of calculating and representing analytical errors provide reasonable context for comparison of measurements made with different techniques. However, we acknowledge that there are uncharacterized uncertainties which may limit the strength of our interpretations.

4.1.2.1. $\delta^{34}S$ of CRS extract compared to individual pyrite grains. CRS extraction captures as silver sulfide not only structural sulfide in pyrite, but also structural sulfide in other metal-sulfide compounds, as well as elemental sulfur, polysulfide, and organo-sulfur compounds (Canfield et al., 1986; Fossing and Jørgensen, 1989). The isotopic composition of each of these particular phases may represent a snapshot of sulfide precipitation at a given depth below the sediment–water interface where sulfide was scavenged by available reactive species, or they may represent precipitation from a homogenized pool of sulfide from multiple depths and sources when pore space was still interconnected and transport via diffusion and advection was possible. Individual grains, or growth zones in individual grains, will always be the former: a snapshot, rather than a spatial and temporal integration of pore fluid chemistries. If the window for pyrite formation was brief and spatially restricted to the same pore fluids as produced other sulfide precipitates, individual grains of pyrite (measured via SIMS) may yield very similar $\delta^{34}S$ values to CRS extracts (measured via EA-IRMS). However, it is difficult to judge how similar without paired CRS and SIMS measurements of the same samples, which we were unable to obtain for this study due to low CRS yields.

Furthermore, SIMS measurements are affected by the interaction of the primary and secondary ion beams with the lattice structure of the mineral being analyzed, and any inclusions or discord in that lattice structure (i.e., matrix effects). These matrix effects can be controlled for only if the matrix of a sample of unknown isotopic composition is identical to the matrix of a standard of known isotopic composition measured in series. Uncharacterized matrix effects may produce differences between "true" and measured isotopic composition.

4.1.2.2. $\delta^{34}S$ of sulfate analyzed via ICP-MS compared to EA-IRMS. Stringent procedures for purification and contamination reduction are undertaken for small amounts of sulfate in preparation for ICP-MS measurements. These procedures are not as stringent for less analyte-limited measurements via EA-IRMS, meaning there may be additional contributors to the sulfate signal measured by EA-IRMS that may affect $\delta^{34}S$ values but which are not considered "contaminants" by our measurement criteria. Possible contributors include: organic matter inclusions which were not leached during washing and acid digestion.

Thus, different analytical techniques may produce systematic differences in isotopic measurements that are beyond the ability of blanks, standards, and contamination screening to identify and control. Such systematic differences may be smaller than the calculated analytical errors for each data type, but — particularly for such a small dataset — they should be remembered and the data interpreted with some reserve.

4.2. Sulfur cycling recorded by carbonate-cemented textures of the Salitre Fm

Non-phosphatic textures of the Salitre Formation include calcite- and dolomite-cemented grainstone and mudstone between stromatolites and adjacent to stromatolite buildups, as well as calcite- and dolomite-cemented stromatolitic boundstone (Fig. 3). Structural sulfate in sampled calcite and dolomite cements associated with oolitic grainstone and laminated mudstone yielded a wide range of $\delta^{34}S$ values, between roughly 19 and 38 ‰ (VCDT) — see Table 1 and Fig. 5. Structural sulfide in pyrite, measured as CRS, which was associated with carbonate-cemented laminated mudstone and carbonate-cemented digitate stromatolites yielded $\delta^{34}S$ values around 7 ‰ (VCDT). $\Delta^{34}S$ in measured carbonate-cemented textures had a range of about 12 to 31 ‰. This range of values is consistent with the range of kinetic isotope effects associated with microbial sulfate reduction. This is to say that: microbial sulfate reduction alone can explain $\Delta^{34}S$ in pore fluids at the time carbonate cements were forming. Sulfur disproportionation and sulfide oxidation may have also occurred in pore fluids at the same time, or even before the sampled sediments were buried below the chemocline and cements precipitated, but the fractionation effects of these metabolisms may not have been as prevalent at the moment captured by the mineralization of carbonate and pyrite. (Note: "prevalence" is a function of metabolic rates, which may itself be a function of cell abundance and/or average metabolic efficiency of a given population of cells).

4.3. Sulfur cycling in CFA cement-forming sediments of the Salitre Fm

Phosphatic textures of the Salitre Formation are defined by the predominance of cryptocrystalline CFA cement, including the laminae of phosphatic digitate stromatolites (Fig. 3). Structural sulfate in CFA cement samples yielded $\delta^{34}S$ of 30–34 ‰ - see Table 1 and Fig. 5. Structural sulfide in pyrite associated with CFA-cemented textures was too low in abundance to yield a measurable mass of CRS, and so individual pyrite crystals and aggregates of pyrite crystals were measured via SIMS from a single sample: *FuroX_3330*. These pyrites yielded $\delta^{34}S$ between about 18 and 39 ‰. $\Delta^{34}S$ in CFA-cemented facies is small: between −5 and 12 ‰. This small fractionation, and possible reverse fractionation, is notably different from that observed in the carbonate-cemented facies. It may be consistent with a scenario in which sulfide oxidation was also prevalent in pore fluids - such that some significant fraction of the ^{34}S-depleted sulfide produced via microbial sulfate reduction was converted to sulfate and the remaining sulfide pool correspondingly ^{34}S-enriched. It may also be consistent with a scenario

in which vigorous microbial sulfide oxidation pushed pyrite mineralization deeper into the sediments, such that pyrite d34S reflects the influence of microbial sulfate reduction on a dwindling, isotopically distilled sulfate pool.

Alternatively, it is possible that the measured CFA -associated pyrite was not representative of biogenic sulfide in sediment pore waters and instead resulted from thermochemical reduction of sulfate during late-stage diagenesis at temperatures >110 °C (Cui et al., 2018), temperatures well within the range experienced by the measured rocks (Sanders et al., 2023). However, carbonate-cemented textures in these samples experienced the same thermal history as the CFA-cemented samples - being within centimeters to meters of one another at the same or similar stratigraphic levels, in the same localities - and we found no ^{34}S-enriched CRS measurements among samples from the carbonate-cemented textures. Thus, we find that a hydrothermal source for the pyrite sulfide observed here unlikely.

In the Sete Lagoas Formation, the corollary of the Salitre Formation representing sedimentation in a more southern sub-basin of the São Francisco Craton's Ediacaran sea (Drummond et al., 2015; Okubo et al., 2018; Sanders and Grotzinger, 2021), bulk CAS and CRS measurements from carbonate rock unaffiliated with phosphatic cements or intraclasts both yielded high δ^{34}S values, around 30–50 ‰ VCDT (Okubo et al., 2022). These values were found to be consistent with models in which low-abundance seawater sulfate in restricted pore waters undergoes isotopic distillation. While this may have applied broadly to the more northern Salitre Formation as well, the texture-specific measurements of CAS, PAS, CRS, and pyrite crystals presented here allow us to distinguish sulfur isotope systematics in phosphogenetic microenvironments from those in non-phosphogenetic microenvironments. This distinction could illuminate how the ecology of marine sediments determined the spatial distribution of phosphogenesis.

Sample *FuroX_3340* was the only sample in which it was possible to measure both PAS and CAS (see Fig. 2, CBPM Core 10). CFA-cemented stromatolite laminae and carbonate-cemented inter-stromatolite fill from this sample yielded $\delta^{34}S_{PAS}$ of 33.42 ± 0.28 ‰ and $\delta^{34}S_{CAS}$ of 26.59 ± 0.23 ‰, respectively. These values are similar enough - considering the variability among δ^{34}S in the same mineral phases within the same samples - that we consider neither CAS nor PAS to be substantially ^{34}S-

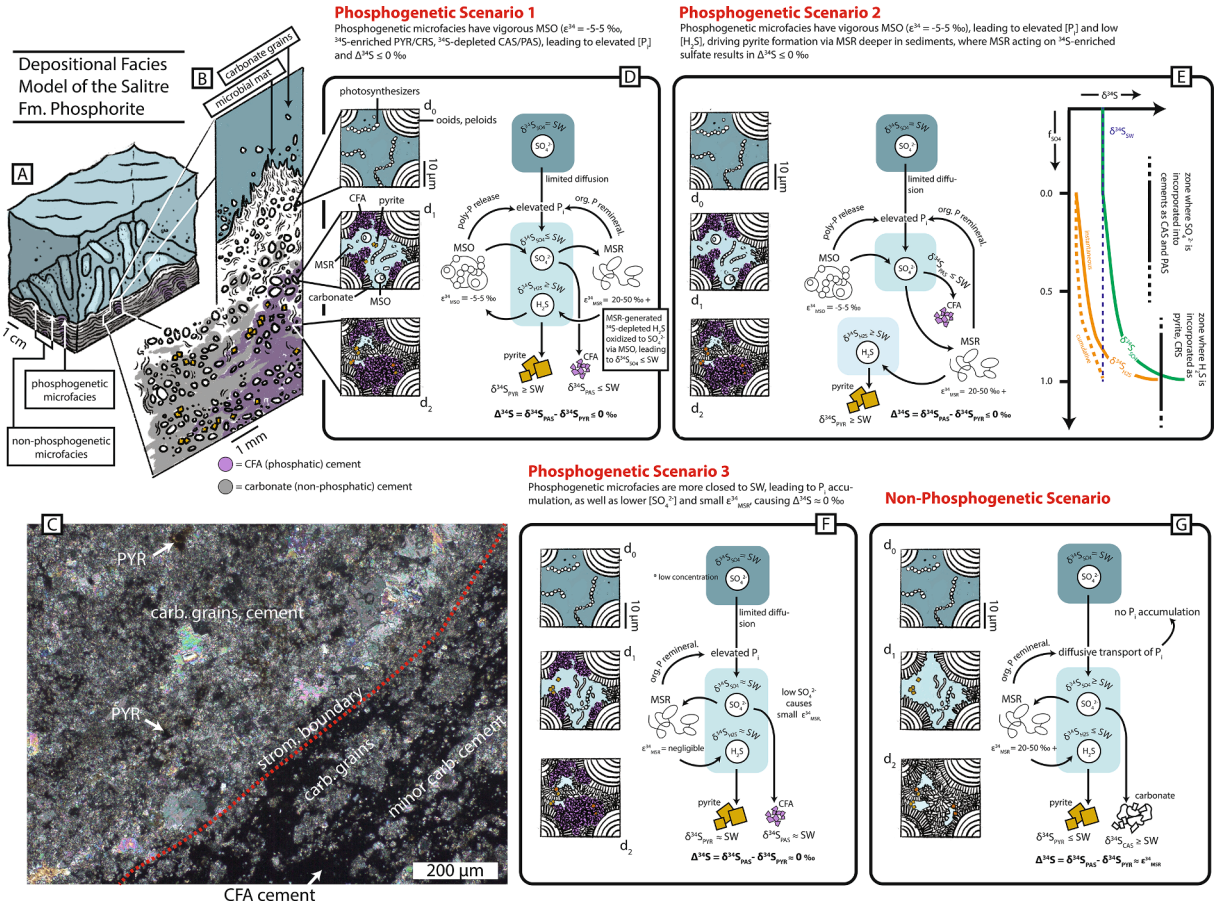

Fig. 6. Schematic diagram depicting possible differences in fluid chemistry during early diagenesis which are consistent with the observed differences in $\delta^{34}S_{PYR,CRS}$ and $\delta^{34}S_{PAS,CAS}$ in phosphogenetic (D-F)-) and non-phosphogenetic (G) microfacies of the Salitre Fm. (A) A cartoon depicting our depositional facies model of the Salitre Formation phosphorite, with phosphogenetc and non-phosphogenetic microfacies indicated — occurring within centimeters to millimeters of one another. (B) A cartoon view of an enlarged cross section of immediately adjacent phosphogenetic and non-phosphogenetic microfacies, at the flanks of a growing stromatolite. (C) A representative transmitted-light photomicrograph (XPL, such that CFA cement is opaque), capturing carbonate- and CFA-cemented fabrics at the flanks of a digitate stromatolite from the Aristeia locality. Cross-sectional depictions of processes occurring in small pore volumes at depths d_0, d_1, and d_2 below the sediment–water interface in (A-B), such as might produce the fabrics in (C), are included in parts (D-G): (D) A simplified model for the relationship between biogeochemical sulfur cycling and phosphogenesis according to Scenario 1, in which phosphogenesis is enabled by more vigorous microbial sulfide oxidation (MSO) in partially restricted pore spaces, and re-oxidation of MSR-generated 34S-depleted sulfide by MSO is responsible for $\Delta^{34}S \leq 0$ ‰. (E) A simplified model for Scenario 2, in which phosphogenesis is enabled by more vigourous MSO, while pyrite formation is simultaneously driven deeper into sediments where MSR acts on 34S-enriched SO4. (F) Simplified model of Scenario 3, in which pore volumes in phosphogenetic microfacies may have become so restricted, and the concentration of sulfate so low, that the isotope effect of MSR became small and the δ^{34}S of the sulfate and sulfide pools are more similar. (G) A simplified depiction of carbonate cementation and no phosphogenesis, enabled by comparatively open-system conditions at comparable depths below sediment water interface. See text for further explanation.

enriched relative to the other. Phosphatic crusts in which $\delta^{34}S_{PAS} < \delta^{34}S_{seawaterSO4}$ have been interpreted as evidence of microbial sulfide oxidation in modern phosphogenetic environments (Arning et al., 2009). However, it seems unlikely that $\delta^{34}S_{CAS}$ as measured in this study (i.e., within pore cements) is truly representative of seawater sulfate $\delta^{34}S$. Rather, it seems likely that $\delta^{34}S_{CAS}$ and $\delta^{34}S_{PAS}$ in co-occurring CFA and carbonate cements simply represent the same pool of pore water sulfate during cementation.

4.4. Sulfur cycling and phosphogenesis in the Salitre Fm

Carbonate-cemented textures and CFA-cemented textures of the Salitre Formation preserve different $\Delta^{34}S$. In carbonate-cemented textures, CAS was generally ^{34}S-enriched with respect to pyrite extracted as CRS: $\Delta^{34}S = 12$ to 31 ‰, where the range reflects the variability among CAS measurements and among CRS measurements. In CFA-cemented textures - i.e., phosphatic textures - PAS and pyrite crystals had more similar sulfur isotope compositions: $\Delta^{34}S = -5$ to 12 ‰. This suggests that there may have been a significant difference in sulfur-cycling dynamics between carbonate-precipitating and phosphate-precipitating textures. There are multiple plausible scenarios that could explain these differences. These are expounded below.

4.4.1. Scenario 1: Phosphogenetic microfacies have elevated rates of microbial sulfide oxidation, leading to elevated [P_i] and $\Delta^{34}S \leq 0$ ‰

In this *Scenario 1* (Fig. 6D): Phosphogenesis is enabled by more vigorous microbial sulfide oxidation (MSO) in partially restricted pore spaces. Fig. 6 depicts the variation in aqueous chemistry and mineralization at increasing depths below the sediment–water interface (depth = d). At depth d_0, the pore volume is filled with fluids of a similar chemical and isotopic composition to the water column immediately above the sediment–water interface; and sufficient light is available for microorganisms performing oxygenic photosynthesis (i.e., cyanobacteria). Phosphogenetic (Fig. 6D–F) and non-phosphogenetic (Fig. 6G) microfacies may evolve from the same conditions near the sediment–water interface at d_0 — having the same pore fluid chemistry, and carbonate sediments. At depth d_0, $\delta^{34}S$ of pore fluid sulfate is similar to that of ambient seawater (SW). It is at depths d_1 and d_2 below the sediment–water interface that differences may emerge which produce phosphatic cements and a relatively ^{34}S-enriched sulfide pool.

In phosphogenetic microfacies (e.g., Fig. 6D), vigorous (higher) rates of microbial sulfide oxidation may have been performed by microorganisms analogous to modern *Beggiatoa* or *Thimargarita,* which accumulate excess phosphate as an alternative metabolic strategy under euxinic conditions (Brock and Schulz-Vogt, 2011). Such polyphosphate-accumulating organisms re-oxidize ^{34}S-depleted sulfide produced by microbial sulfate reduction or MSR ($\varepsilon^{34}_{MSR} \approx 20$ to 50 ‰ +) to sulfate. This metabolic pathway (having $\varepsilon^{34}_{MSO} \approx -5$ to 5 ‰) results in a relatively ^{34}S-enriched sulfide pool ($\delta^{34}S_{H2S} \geq \delta^{34}S_{SW}$) and a more ^{34}S-depleted sulfate pool ($\delta^{34}S_{SO4} \leq \delta^{34}S_{SW}$), which is reflected in the $\delta^{34}S$ values of structural sulfate in phosphatic cements (PAS) and pyrite (PYR, CRS) precipitated at d_1 and d_2. In non-phosphogenetic microfacies (Fig. 6G), there may have been a lower rate of MSO, perhaps due to more unrestricted communication with the seawater sulfate pool and more oxygenating fluids, resulting in $\delta^{34}S_{SO4} > \delta^{34}S_{SW}$ and $\delta^{34}S_{H2S} \leq \delta^{34}S_{SW}$, which would be captured in the $\delta^{34}S$ values of structural sulfate in carbonate cements (CAS) and pyrite (PYR, CRS) precipitated at d_1 and d_2.

In modern phosphogenetic environments, microbial sulfide oxidation appears to be instrumental in enabling early phosphate mineralization in marine sediments. Biomarkers associated with polyphosphate-accumulating sulfide oxidizers are more abundant in phosphogenetic sediments than co-occuring non-phosphogenetic sediments (Arning et al., 2009). Actively growing phosphatic crusts incorporate body fossils of both sulfate-reducing and sulfide-oxidizing microorganisms (Schulz and Schulz, 2005; Arning et al., 2009; Goldhammer et al., 2010; Bailey et al., 2013). Cultures of sulfide-oxidizing organisms from modern phosphogenetic environments can be induced to raise aqueous phosphate concentrations sharply under conditions of high sulfide concentration (Schulz and Schulz, 2005; Brock and Schulz-Vogt, 2011).

There is evidence of sulfide oxidizing metabolisms at work in ancient phosphogenetic settings. Microbial fossils with morphologies and size distributions comparable to modern polyphosphate-accumulating microorganisms have been identified in the Ediacaran phosphatic stromatolites of Central and Northern India (Bengtson et al., 2017; Sallstedt et al., 2018). The Doushantuo Formation of Southern China also contains microbial fossils which resemble modern sulfide-oxidizing microorganisms (Bailey et al., 2007, 2013), as does the Miocene Monterey Formation in the Western United States (Bailey et al., 2013). Lipid biomarkers associated with sulfide oxidizing bacteria have been identified in the phosphorite deposits of the Mishash/Ghareb Formation in Israel (Alsenz et al., 2015).

However, there are few comparative studies of ancient phosphorites that demonstrate paleoenvironmental and paleoecological differences between phosphogenetic and non-phosphogenetic facies, and which demonstrate the presence of sulfide-oxidizing microorganisms in the former and absence in the latter. It is therefore significant that the isotopic data presented in this study do not nullify the hypothesis that differences in sulfur-metabolizing microbial communities can begat differences in the prevalence of early phosphate mineralization in the ancient ocean.

4.4.2. Scenario 2: Phosphogenetic microfacies have elevated rates of microbial sulfide oxidation, leading to elevated [P_i] and delayed pyrite mineralization, $\Delta^{34}S \leq 0$ ‰

In *Scenario 2* (Fig. 6E), as in scenario 1, vigorous MSO under episodically euxinic conditions in partially restricted pore space may explain the precipitation of phosphatic cements at d_1 and d_2. In this case, however, the ^{34}S-enrichment of the sulfide pool as preserved by structural sulfur in pyrite is explained not by MSO re-oxidizing ^{34}S-depleted sulfide and its isotope fractionating effects, but rather: by the rapid consumption of sulfide by MSO at d_1).

If sulfide generated via MSR is rapidly consumed by MSO at d_1, there may not be sufficient concentrations of sulfide available for reaction with free Fe^{2+}, and therefore no precipitation of Fe-sulfide minerals like pyrite. Rather, precipitation of Fe-sulfides is driven deeper in the sediments (d_2 or beyond), where the continued operation of MSR under increasingly closed-system conditions would result in precipitation of pyrite from an increasingly ^{34}S-enriched sulfide pool.

4.4.3. Scenario 3: Phosphogenetic microfacies are more closed to seawater, leading to P_i accumulation, as well as lower [SO_4^{2-}] and small ε^{34}_{MSR}, causing $\Delta^{34}S \approx 0$ ‰

In *Scenario 3* (Fig. 6F), pore volumes in phosphogenetic microfacies may have become so restricted, and the concentration of sulfate so low, that the isotope effect of MSR became small and the $\delta^{34}S$ of the sulfate and sulfide pools are more similar. In this scenario, $\delta^{34}S_{H2S}$ cannot be higher than $\delta^{34}S_{SW}$. Closure/restriction of pore volumes would also explain the retention of dissolved phosphate in pore fluids, after being liberated from organic matter via MSR, which would allow for the precipitation of phosphatic cements wherever the degree of closure of a given pore volume passes a certain threshold below the sediment–water interface. Physical restriction of pore space may have resulted from a number of factors, including geometry of stromatolite margins as effected by flow velocity and sedimentation rates, as suggested by previous workers (Caird et al., 2017). Since the spatial extent of early phosphate cements is limited to digitate stromatolite morphologies in the Salitre Fm., this scenario — wherein restriction of pore space to sulfate transport controls distribution of phosphogenetic pore fluid chemistries — seems tenable. However, the occurrence of carbonate-cemented digitate stromatolites is not explained by this model, and there is no clear textural evidence that the geometry of grains and their

interstitial spaces varies significantly between phosphatic and non-phosphatic microfacies. Nevertheless, Scenario 3 is consistent with the correlation of phosphatic cement mineralogy and low $\Delta^{34}S$.

5. Conclusions

5.1. Sulfur isotope compositions differ between phosphatic and non-phosphatic microfacies

Sulfur isotope compositions of cement phases in phosphatic microfacies of the Salitre Fm. differ from those of non-phosphatic facies. Specifically: CAS and PAS yield similar $\delta^{34}S$ (~20–40 ‰) values in phosphatic and non-phosphatic facies; but $\delta^{34}S$ of pyrite and CRS tended to be more similar to PAS in phosphatic facies, and lighter than CAS by tens of ‰ in non-phosphatic facies. These values, and their textural contexts, are consistent with a scenario in which the spatial distribution of phosphogenesis in the Ediacaran Salitre paleobasin was controlled by the spatial distribution of environmental or ecological factors which also impacted sediment pore water sulfur cycling. There are several plausible scenarios which could explain the correlation of the observed variation in the isotopic record of sulfur cycling with variations in the patterns of phosphate mineralization.

Phosphate mineralization may have occurred in pore volumes containing larger or more rapidly metabolizing populations of sulfide-oxidizing microorganisms, if these microorganisms — like their modern analogs — accumulated polyphosphate and released inorganic phosphate into pore fluids in response to episodic, local euxinia (Schulz and Schulz, 2005; Brock and Schulz-Vogt, 2011). High rates of sulfide oxidation may result in similar pyrite/CRS and PAS/CAS values by (1) re-oxidizing ^{34}S-depleted sulfide derived from MSR to sulfate, (2) employing metabolic pathways which impart a fractionation effect which enriches the sulfide pool with respect to ^{34}S, and/or (3) driving pyrite mineralization deeper below the sediment water interface, such that microbial sulfate reduction under closed-system conditions acts on a more ^{34}S-enriched sulfate pool.

Phosphate mineralization may have also occurred in pore volumes that were more restricted with respect to the diffusion of sulfate and inorganic phosphate, due to the closure of pore space by microbial filaments and extracellular polymers and related variations in the distribution of sediment at the seafloor, manifested as digitate stromatolite morphology. However, if phosphogenesis was dependent only on physical restriction of pore volumes, another explanation must be provided for the lack of correlation between cement mineralogy and sediment/pore geometry, and the occurrence of non-phosphatic digitate stromatolites.

Thus, our data are consistent with, but do not necessitate, a role for polyphosphate-accumulating sulfide-oxidizing microorganisms in Ediacaran phosphogenesis — as observed in modern phosphogenetic settings.

5.2. Broader implications for interpretation of the phosphorite record

The geologic record is like a book written in minerals, textures, and isotope fractionations rather than paper and ink. Some chapters are faithful, complete accounts of historical events. Others are profoundly subjective and limited by the geographic and ecological scope of their authors. Understanding the mechanisms by which the record was formed — taphonomy — is thus a sort of literary analysis through which we interrogate the context and biases of the authors and the medium of the writing.

In this study, we question the relative influence of different sulfur-metabolizing microorganisms as authors and editors of this particular volume of geobiological history: the Precambrian-Cambrian boundary. If phosphogenesis during this period was indeed a function of the changeable, localized metabolic habits of sulfide-oxidizing bacteria, then perhaps the occurrence of sedimentary phosphate deposits and their fossil biota should be regarded as records of microbial metabolic processes — as much as they are regarded as records of global perturbations to nutrient cycling and oxygen availability.

Data availability

Data are available through Mendeley Data at https://doi.org/10.17632/2bf8vmrgw8.1. Raw, unprocessed data are available upon request submitted to the corresponding author.

CRediT authorship contribution statement

Cecilia Sanders: Writing – review & editing, Writing – original draft, Visualization, Project administration, Methodology, Investigation, Formal analysis, Conceptualization. **Theodore Present:** Writing – review & editing, Supervision, Methodology, Formal analysis, Data curation. **Selva Marroquin:** Writing – review & editing, Supervision. **John Grotzinger:** Supervision, Resources, Funding acquisition.

Declaration of competing interest

The authors declare that they have no known competing financial interests or personal relationships that could have appeared to influence the work reported in this paper.

Acknowledgements

The authors extend their gratitude to Wu Fenfang, Guan Yunbin, Grecia “Grace” Ames, and Antoine Cremiere of Caltech’s Division of Geological and Planetary Sciences, for the gift of their expertise, and their patience, as we learned new techniques on new analytical instruments.

We also express our gratitude for the friendship and collaboration with the students, professors, and researchers of the Laboratório de Análises de Minerais e Rochas (LAMIR) e Laboratório de Análises de Bacias (LABAP) da Universidade Federal do Paraná, as well as our collaborators from the Universidade Federal do Bahia, without whom we could not have collected our samples and immersed ourselves in the geology and culture of the studied region. We are also wholly indebted to the farmers, miners, educators, and conservationists of the Chapada Diamantina and Cavernas do Peruaçu regions for their guidance and expertise.

We also wish to thank the reviewers and editors for helpful, insightful comments. We also acknowledge that this work was supported primarily by the National Science Foundation Graduate Research Fellowship Program (NSF GRFP), and the Simons Collaboration on the Origins of Life (SCOL).

Lastly, we humbly acknowledge the Xakriabá, the communities of and surrounding the historic Quilombo da Gruta dos Brejões, as well as other indigenous peoples whose names and identities may have been lost to colonialism and occupation, on whose land this work relies.

Appendix A. Supplementary material

Two supplementary figures are provided which may further illuminate the analytical techniques and data reduction methods utilized in this study. Fig. S1 contains a schematic of the analytical pipeline: powder sample collection, cleaning and purification, and mass spectrometry. Fig. S2 contains an annotated illustration of the criteria by which some measurements were excluded from the final analyzed dataset, and the possible implications of those criteria for results and interpretation. Supplementary material to this article can be found online at https://doi.org/10.1016/j.gca.2023.12.033.

References

Alkmim, F.F., Martins-Neto, M.A., 2012. Proterozoic first-order sedimentary sequences of the São Francisco craton, eastern Brazil. Mar. Pet. Geol. 33, 127–139.

Alsenz, H., Illner, P., Ashckenazi-Polivoda, S., Meilijson, A., Abramovich, S., Feinstein, S., Almogi-Labin, A., Berner, Z., Püttmann, W., 2015. Geochemical evidence for the link between sulfate reduction, sulfide oxidation and phosphate accumulation in a late cretaceous upwelling system. Geochem. Trans. 16, 1–13.

Anschutz, P., Zhong, S., Sundby, B., Mucci, A., Gobeil, C., 1998. Burial efficiency of phosphorus and the geochemistry of iron in continental margin sediments. Limnol. Oceanogr. 43, 53–64.

Arning, E.T., Birgel, D., Brunner, B., Peckmann, J., 2009. Bacterial formation of phosphatic laminites off Peru. Geobiology 7, 295–307.

Bailey, J.V., Joye, S.B., Kalanetra, K.M., Flood, B.E., Corsetti, F.A., 2007. Evidence of giant sulphur bacteria in Neoproterozoic phosphorites. Nature 445, 198–201.

Bailey, J.V., Corsetti, F.A., Greene, S.E., Crosby, C.H., Liu, P., Orphan, V.J., 2013. Filamentous sulfur bacteria preserved in modern and ancient phosphatic sediments: implications for the role of oxygen and bacteria in phosphogenesis. Geobiology 11, 397–405.

Bengtson, S., Sallstedt, T., Belivanova, V., Whitehouse, M., 2017. Three-dimensional preservation of cellular and subcellular structures suggests 1.6 billion-year-old crown-group red algae. PLoS Biol. 15, 1–38.

Boudreau, B.P., Westrich, J.T., 1984. The dependence of bacterial sulfate reduction on sulfate concentration in marine sediments. Geochim. Cosmochim. Acta 48, 2503–2516.

Bradley, A.S., Leavitt, W.D., Schmidt, M., Knoll, A.H., Girguis, P.R., Johnston, D.T., 2016. Patterns of sulfur isotope fractionation during microbial sulfate reduction. Geobiology 14, 91–101.

Brock, J., Schulz-Vogt, H.N., 2011. Sulfide induces phosphate release from polyphosphate in cultures of a marine Beggiatoa strain. ISME J. 5, 497–506.

Brunner, B., Bernasconi, S.M., 2005. A revised isotope fractionation model for dissimilatory sulfate reduction in sulfate reducing bacteria. Geochim. Cosmochim. Acta 69, 4759–4771.

Caird, R.A., Pufahl, P.K., Hiatt, E.E., Abram, M.B., Rocha, A.J.D., Kyser, T.K., 2017. Ediacaran stromatolites and intertidal phosphorite of the Salitre Formation, Brazil: phosphogenesis during the Neoproterozoic Oxygenation Event. Sediment. Geol. 350, 55–71.

Canfield, D.E., 2019. Biogeochemistry of sulfur isotopes. Stable Isot. Geochem. 43, 607–636.

Canfield, D.E., Raiswell, R., Westrich, J.T., Reaves, C.M., Berner, R.A., 1986. The use of chromium reduction in the analysis of reduced inorganic sulfur in sediments. Chem. Geol. 54, 149–155.

Canfield, D.E., Farquhar, J., Zerkle, A.L., 2010. High isotope fractionations during sulfate reduction in a low-sulfate euxinic ocean analog. Geology 38, 415–418.

Canfield, D.E., Teske, A., 1996. Late proterozoic rise in atmospheric oxygen concentration inferred from phylogenetic and sulphur-isotope studies. Nature 382, 127–132.

Caxito, F.d.A., Halverson, G.P., Uhlein, A., Stevenson, R., Dias, T.G., Uhlein, G.J., 2012. Marinoan glaciation in east central Brazil. Precambrian Res. 200–203, 38–58.

Cline, J.D., 1969. Spectrophotometric determination of hydrogen sulfide in natural waters. Assoc. Sci. Limnol. Oceanogr. 14, 454–458.

Cook, P.J., 1992. Phosphogenesis around the Proterozoic-Phanerozoic transition. J. - Geol. Soc. 149, 615–620.

Cordani, U.G., Sato, K., 1999. Crustal evolution of the South American platform, based on Nd isotopic systematics on granitoid rocks. Episodes 22, 167–173.

Creveling, J.R., Knoll, A.H., Johnston, D.T., 2014. Taphonomy of Cambrian phosphatic small shelly fossils. Palaios 29, 295–308.

Crosby, C.H., Bailey, J.V., 2012. The role of microbes in the formation of modern and ancient phosphatic mineral deposits. Front. Microbiol. 3, 1–7.

Cui, H., Kitajima, K., Spicuzza, M.J., Fournelle, J.H., Denny, A., Ishida, A., Zhang, F., Valley, J.W., 2018. Questioning the biogenicity of Neoproterozoic superheavy pyrite by SIMS. Am. Mineral. 103, 1362–1400.

Dale, A.W., Brüchert, V., Alperin, M., Regnier, P., 2009. An integrated sulfur isotope model for Namibian shelf sediments. Geochim. Cosmochim. Acta 73, 1924–1944.

Dalton de Souza, J., de Melo, R.C., Kosin, M., de Jesus, J.D.A., Ramos, M.A.B., Delgado, I. d,M., dos Santos, R.A., das Neves, J.P., Britto, E.C., Teixeira, L.R., Sampaio, Antonio Rabelo Guimarães, J.T., Vieira Bento, R., Borges, V.P., Martins, A.A., Arcanjo, J.B., Loureiro, H.S., Angelim, L.A.A., Monteiro, M.A.S., de Souza, N.P., Monteiro, S.R.J., dos S Fuezi, V.M., Borges, M.P., da Costa, J.M., de Lima, C.L., 2003. *Mapa geologico do Estado da Bahia.*, CPRM - Serviço Geológico do Brasil, Governo do Estado da Bahia, Ministerio de Minas e Energia, Companhia Baiana de Pesquisa Mineral.

Defforey, D., Paytan, A., 2018. Phosphorus cycling in marine sediments: advances and challenges. Chem. Geol. 477, 1–11.

Demidenko, Y.E., Zhegallo, E.A., Parkhaev, P.Y., Shuvalova, Y.V., 2003. Age of phosphorites from the Khubsugul basin (Mongolia). Dokl. Earth Sci. 389, 317–321.

Drummond, J.B.R., Pufahl, P.K., Porto, C.G., Carvalho, M., 2015. Neoproterozoic peritidal phosphorite from the Sete Lagoas Formation (Brazil) and the Precambrian phosphorus cycle. Sedimentology 62, 1978–2008.

Eagle, R.A., Schauble, E.A., Tripati, A.K., Tütken, T., Hulbert, R.C., Eiler, J.M., 2010. Body temperatures of modern and extinct vertebrates from 13C–18O bond abundances in bioapatite. Proc. Natl. Acad. Sci. U.S.A. 107, 10377–10382.

Farquhar, J., Johnston, D.T., Wing, B.A., Habicht, K.S., Canfield, D.E., Airieau, S., Thiemens, M.H., 2003. Multiple sulphur isotopic interpretations of biosynthetic pathways: implications for biological signatures in the sulphur isotope record. Geobiology 1, 27–36.

Fike, D.A., Grotzinger, J.P., 2008. A paired sulfate–pyrite d34S approach to understanding the evolution of the Ediacaran-Cambrian sulfur cycle. Geochim. Cosmochim. Acta 72, 2636–2648.

Filippelli, G.M., 2011. Phosphate rock formation and marine phosphorus geochemistry: the deep time perspective. Chemosphere 84, 759–766.

Föllmi, K., 1996. The phosphorus cycle, phosphogenesis phosphate-rich deposits. Earth-Science Rev. 40, 55–124.

Fonseca, M.A., Pinto, C.P., da Silva, M.A., Ribeiro, J.H., Tuller, M.P., Signorelli, N., Baltazar, O.F., Féboli, W.L., Borges, A.J., Augusto, M.F., Dias, P.S.A., de Souza, R.G. B., Costa, E.d.A.C., Cândido, M., Pinheiro, M.A.P., da Silva, L.C., Noce, C.M., Assunção Martins dos Santos, E.d, Xavier, A.P.M., Ilambwetsi, A.M., Cieira, C.S., Rocha de Rezende, C., da Silva, D.P., Alves, E.S., da Silva, E.A.S., Santos, L.J.H., Schmit de Lima, V., 2014. *Mapa Geológico do Estado de Minas Gerais.*, CPRM - Serviço Geológico do Brasil, Governo de Minas, Ministerio de Minas e Energia, Companhia de Desenvolvimento Econômico de Minas Gerais.

Fossing, H., Jørgensen, B.B., 1989. Measurement reduction of a single-step chromium method Evaluation. Biogeochemistry 8, 205–222.

Goldhammer, T., Brüchert, V., Ferdelman, T.G., Zabel, M., 2010. Microbial sequestration of phosphorus in anoxic upwelling sediments. Nat. Geosci. 3, 557–561.

Gomes, M.L., Johnston, D.T., 2017. Oxygen and sulfur isotopes in sulfate in modern euxinic systems with implications for evaluating the extent of euxinia in ancient oceans. Geochim. Cosmochim. Acta 205, 331–359.

Guimarães, J.T., Misi, A., Pedreira, A.J., Dominguez, J.M.L., 2011. The Bebedouro Formation, Una Group, Bahia (Brazil). Geol. Soc. Mem. 36, 503–508.

Habicht, K.S., Canfield, D.E., 2001. Isotope fractionation by sulfate-reducing natural populations and the isotopic composition of sulfide in marine sediments. Geology 29, 555–558.

Habicht, K.S., Canfield, D.E., Rethmeier, J., 1998. Sulfur isotope fractionation during bacterial reduction and disproportionation of thiosulfate and sulfite. Geochim. Cosmochim. Acta 62, 2585–2595.

Halverson, G.P., Hurtgen, M.T., 2007. Ediacaran growth of the marine sulfate reservoir. Earth Planet. Sci. Lett. 263, 32–44.

Harrison, A.G., Thode, H.G., 1958. Mechanism of the bacterial reduction of sulphate from isotope fractionation studies. Trans. Faraday Soc. 54, 84–92.

Hurtgen, M.T., Arthur, M.A., Halverson, G.P., 2005. Neoproterozoic sulfur isotopes, the evolution of microbial sulfur species, and the burial efficiency of sulfide as sedimentary pyrite. Geology 33, 41–44.

Johnson, D.L., Present, T.M., Li, M., Shen, Y., Adkins, J.F., 2021. Carbonate associated sulfate (CAS) δ34S heterogeneity across the End-Permian Mass Extinction in South China. Earth Planet. Sci. Lett. 574, 117172.

Johnston, D.T., Farquhar, J., Wing, B.A., Kaufman, A.J., Canfield, D.E., Habicht, K.S., 2005. Multiple sulfur isotope fractionations in biological systems: A case study with sulfate reducers and sulfur disproportionators. Am. J. Sci. 305, 645–660.

Kaplan, I.R., Rafter, T.A., 1958. Fractionation of stable isotopes of sulfur by thiobacilli. Science 80-.). 127, 517–518.

Kita, N.T., Huberty, J.M., Kozdon, R., Beard, B.L., Valley, J.W., 2011. High-precision SIMS oxygen, sulfur and iron stable isotope analyses of geological materials: accuracy, surface topography and crystal orientation. Surf. Interface Anal. 43, 427–431.

Kozdon, R., Kita, N.T., Huberty, J.M., Fournelle, J.H., Johnson, C.A., Valley, J.W., 2010. In situ sulfur isotope analysis of sulfide minerals by SIMS: precision and accuracy, with application to thermometry of ~3.5Ga Pilbara cherts. Chem. Geol. 275, 243–253.

Kuchenbecker, M., Luis, H., Galvão, D., 2011. Caracterização estrutural e considerações sobre a evolução tectônica da Formação Salitre na porção central da Bacia de Irecê, norte do Cráton do. Geonomos 19, 42–49.

Laakso, T.A., Sperling, E.A., Johnston, D.T., Knoll, A.H., 2020. Ediacaran reorganization of the marine phosphorus cycle. Proc. Natl. Acad. Sci. U S. A. 117.

Lesniak, P.M., Lacka, B., Krajewski, K.P., Zawidzki, P., Hladikova, J., 2003. Extreme sulfur isotopic fractionation between sulfate of carbonate fluorapatite and authigenic pyrite in the Neocomian sequence at Wawali, Central Poland. Chem. Geol. 200, 325–337.

Loyd, S.J., Marenco, P.J., Hagadorn, J.W., Lyons, T.W., Kaufman, A.J., Sour-Tovar, F., Corsetti, F.A., 2012. Sustained low marine sulfate concentrations from the Neoproterozoic to the Cambrian: insights from carbonates of northwestern Mexico and eastern California. Earth Planet. Sci. Lett. 339–340, 79–94.

Martins-Neto, M.A., Pedrosa-Soares, A.C., Lima, S.A.A., 2001. Tectono-sedimentary evolution of sedimentary basins from Late Paleoproterozoic to Late Neoproterozoic in the São Francisco craton and Araçuaí fold belt, Eastern Brazil. Sediment. Geol. 141–142, 343–370.

McClellan, G.H., 1980. Mineralogy of carbonate fluorapatites. J. Geol. Soc. 137, 675–681.

Misi, A., Kyle, J.R., 1994. Upper Proterozoic carbonate stratigraphy, diagenesis, and stromatolitic phosphorite formation, Irece Basin, Bahia, Brazil. J. Sediment. Res. A Sediment. Petrol. Process. 64 A, 299–310.

Misi, A., Kaufman, A.J., Veizer, J., Powis, K., Azmy, K., Boggiani, P.C., Gaucher, C., Teixeira, J.B.G., Sanches, A.L., Iyer, S.S.S., 2007. Chemostratigraphic correlation of Neoproterozoic successions in South America. Chem. Geol. 237, 143–167.

Misi, A., Veizer, J., 1998. Neoproterozoic carbonate sequences of the Una Group, Irecê Basin, Brazil: Chemostratigraphy, age and correlations. Precambrian Res. 89, 87–100.

Nathan, Y., Nielsen, H., 1980. Sulfur isotopes in phosphorites. SEPM Spec. Publ. 29, 73–78.

Okubo, J., Muscente, A.D., Luvizotto, G.L., Uhlein, G.J., Warren, L.V., 2018. Phosphogenesis, aragonite fan formation and seafloor environments following the Marinoan glaciation. Precambrian Res. 311, 24–36.

Okubo, J., Kaufman, A.J., Warren, L.V., Evans, M.N., Marroquín, S., Varni, M.A., Misi, A., Bahniuk, A.M., Xiao, S., 2022. The sulfur isotopic consequence of seawater sulfate distillation preserved in the Neoproterozoic Sete Lagoas post-glacial carbonate, eastern Brazil. J. Geol. Soc. London, jgs2021-091.

Papineau, D., 2010. Global biogeochemical changes at both ends of the Proterozoic: Insights from phosphorites. Astrobiology 10, 165–181.

Paris, G., Sessions, A.L., Subhas, A.V., Adkins, J.F., 2013. MC-ICP-MS measurement of δ34S and Δ33S in small amounts of dissolved sulfate. Chem. Geol. 345, 50–61.

Paris, G., Fehrenbacher, E.S., Sessions, A.L., Spero, H.J., Adkins, J.F., 2014. Experimental determination of carbonate-associated sulfate δ34S in planktonic foraminifera shells. Geochem. Geophys. Geosyst. 15, 1452–1461.

Paytan, A., Mclaughlin, K., 2007. The oceanic phosphorus cycle. Chem. Rev. 107, 263–576.

Pellerin, A., Antler, G., Holm, S.A., Findlay, A.J., Crockford, P.W., Turchyn, A.V., Jørgensen, B.B., Finster, K., 2019. Large sulfur isotope fractionation by bacterial sulfide oxidation. Sci. Adv. 5, 1–7.

Poser, A., Vogt, C., Knoller, K., Ahlheim, J., Weiss, H., Kleinsteuber, S., Richnow, H.H., 2014. Stable sulfur and oxygen isotope fractionation of anoxic sulfide oxidation by two different enzymatic pathways. Environ. Sci. Technol. 48, 9094–9102.

Present, T.M., Paris, G., Burke, A., Fischer, W.W., Adkins, J.F., 2015. Large Carbonate Associated Sulfate isotopic variability between brachiopods, micrite, and other sedimentary components in Late Ordovician strata. Earth Planet. Sci. Lett. 432, 187–198.

Present, T.M., Gutierrez, M., Paris, G., Kerans, C., Grotzinger, J.P., Adkins, J.F., 2019. Diagenetic controls on the isotopic composition of carbonate-associated sulphate in the Permian Capitan Reef Complex, West Texas. Sedimentology 66, 2605–2626.

Pruss, S.B., Dwyer, C.H., Smith, E.F., Macdonald, F.A., Tosca, N.J., 2019. Phosphatized early Cambrian archaeocyaths and small shelly fossils (SSFs) of southwestern Mongolia. Palaeogeogr. Palaeoclimatol. Palaeoecol. 513, 166–177.

Reis, H.L.S., Alkmim, F.F., Fonseca, R.C.S., Nascimento, T.C., Suss, J.F., Prevatti, L.D., 2016. The São Francisco Basin. In: Heilbron, M., Cordani, U.G., Alkmim, F.F. (Eds.) The São Francisco Craton, Eastern Brazil: Tectonic Genealogy of a Miniature Continent. Springer, pp. 117–143.

Reis, H.L.S., Suss, J.F., Fonseca, R.C.S., Alkmim, F.F., 2017. Ediacaran forebulge grabens of the southern São Francisco basin, SE Brazil: craton interior dynamics during West Gondwana assembly. Precambrian Res. 302, 150–170.

Richardson, J.A., Newville, M., Lanzirotti, A., Webb, S.M., Rose, C.V., Catalano, J.G., Fike, D.A., 2019. Depositional and diagenetic constraints on the abundance and spatial variability of carbonate-associated sulfate. Chem. Geol. 523, 59–72.

Riciputi, L.R., Paterson, B.A., Ripperdan, R.L., 1998. Measurement of light stable isotope ratios by SIMS: Matrix effects for oxygen, carbon, and sulfur isotopes in minerals. Int. J. Mass Spectrom. 178, 81–112.

Ries, J.B., Fike, D.A., Pratt, L.M., Lyons, T.W., Grotzinger, J.P., 2009. Superheavy pyrite (δ34Spyr > δ34SCAS) in the terminal Proterozoic Nama Group, southern Namibia: a consequence of low seawater sulfate at the dawn of animal life. Geology 37, 743–746.

Sallstedt, T., Bengtson, S., Broman, C., Crill, P.M., Canfield, D.E., 2018. Evidence of oxygenic phototrophy in ancient phosphatic stromatolites from the Paleoproterozoic Vindhyan and Aravalli Supergroups, India. Geobiology 16, 139–159.

Sanders, C.B., Eiler, J.C., Grotzinger, J.P., 2023. Paragenesis of an Ediacaran carbonate-platform phosphorite: constraints from optical petrography and texture-specific clumped isotope paleothermometry. Sediment. Geol. 444, 106316.

Sanders, C., Grotzinger, J., 2021. Sedimentological and stratigraphic constraints on depositional environment for Ediacaran carbonate rocks of the São Francisco Craton: implications for phosphogenesis and paleoecology. Precambrian Res. 363, 106328.

Schulz, H.N., Schulz, H.D., 2005. Large sulfur bacteria and the formation of phosphorite. Science (80-.) 307, 416–418.

Sheldon, R.P., 1981. Ancient marine phosphorites. Annu. Rev. Earth Planet. Sci. 9, 251–284.

Shields, G., Kimura, H., Yang, J., Gammon, P., 2004. Sulphur isotopic evolution of Neoproterozoic-Cambrian seawater: new francolite-bound sulphate δ34S data and a critical appraisal of the existing record. Chem. Geol. 204, 163–182.

Shields, G.A., Strauss, H., Howe, S.S., Siegmund, H., 1999. Sulphur isotope compositions of sedimentary phosphorites from the basal Cambrian of China: implications for Neoproterozoic-Cambrian biogeochemical cycling. J. Geol. Soc. London. 156, 943–955.

Shiraishi, F., Ohnishi, S., Hayasaka, Y., Hanzawa, Y., Takashima, C., Okumura, T., Kano, A., 2019. Potential photosynthetic impact on phosphate stromatolite formation after the Marinoan glaciation: paleoceanographic implications. Sediment. Geol. 380, 65–82.

Southgate P. N. (2005) Proterozoic and Cambrian phosphorites – specialist studies: Middle Cambrian phosphatic hardgrounds, phoscrete profiles and stromatolites and their implications for phosphogenesis. In: Cook, P.J., Shergold J.H. (Eds.) Phosphate Deposits of the World, Vol. 1. Cambridge University Press, pp. 327–351.

Staudt, W.J., Schoonen, M.A.A., 1995. Geochemical Transformations of Sedimentary Sulfur: Sulfate Incorporation into Sedimentary Carbonates. In: ACS Symposium Series, pp. 332–345.

Stolper, D.A., Eiler, J.M., 2016. Constraints on the formation and diagenesis of phosphorites using carbonate clumped isotopes. Geochim. Cosmochim. Acta 181, 238–259.

Sundby, B., Gobeil, C., Silverberg, N., Mucci, A., 1992. The phosphorus cycle in coastal marine sediments. Limnol. Oceanogr. 37, 1129–1145.

Wotte, T., Strauss, H., Fugmann, A., Garbe-Schönberg, D., 2012. Paired δ 34S data from carbonate-associated sulfate and chromium-reducible sulfur across the traditional Lower-Middle Cambrian boundary of W-Gondwana. Geochim. Cosmochim. Acta 85, 228–253.

Xiao, S., Knoll, A.H., 1999. Fossil preservation in the Neoproterozoic Doushantuo phosphorite Lagerstatte, South China. Lethaia 32, 219–238.

Xiao, S., Zhang, Y., Knoll, A.H., 1998. Three-dimensional preservation of algae and animal embryos in a neoproterozoic phosphorite. Nature 391, 553–558.